

Banner appropriate to article type will appear here in typeset article

# Threshold for synchronisation and conditional Lyapunov analysis of large eddy simulations for turbulent flows

Jian Li<sup>1</sup>, Wenwen Si<sup>1</sup>, Yi Li<sup>2†</sup>, Peng Xu<sup>1</sup>

<sup>1</sup>School of Naval Architecture and Maritime, Zhejiang Ocean University, Zhoushan, 316022, China

<sup>2</sup>School of Mathematics and Statistics, University of Sheffield, Sheffield, S3 7RH, UK

(Received xx; revised xx; accepted xx)

The synchronisation between turbulent flows in three dimensional periodic boxes is investigated through conditional and unconditional Lyapunov analyses based on the data obtained with direct numerical simulations and large eddy simulations. By systematic numerical experiments, we find that the leading Lyapunov exponents obtained with large eddy simulations follow the same scaling law as that of filtered perturbations of the real flow, thus should be interpreted as approximations of the latter. Data on the threshold coupling wavenumber for synchronisation show that the synchronisability of coupled turbulent flows is mainly determined by the conditional leading Lyapunov exponents of the slave flow itself, and is insensitive to the nature of the master flow. We present strong evidence to show that the peak wavenumber for the energy spectrum of the leading Lyapunov vector is approximately the same as the threshold wavenumber, corroborating a relationship established recently in rotating turbulence. The threshold wavenumber of large eddy simulations based on canonical subgrid-scale stress models is shown to be different from that of direct numerical simulations, even for the more sophisticated dynamical mixed model. By employing new parametrisation, the threshold wavenumbers are quantified. The care one needs to exercise to interpret the results obtained with large eddy simulations is discussed.

## 1. Introduction

Synchronisation of turbulent flows has been a topic of great interest in recent years. In the simplest form, the technique seeks to reproduce the evolution of one flow in another, by feeding incomplete data obtained from the former into the latter through some coupling mechanism. The technique is at the core of many applications where data assimilation (Kalnay 2003) is used to enhance the control, construction or prediction of instantaneous turbulence field. Typically there are two types of coupling, which have been termed master-slave coupling (Lalescu *et al.* 2013) and nudging coupling (Di Leoni *et al.* 2020) by various authors. In the master-slave coupling, the velocity in a sub-domain from one flow is copied into the other, which drives the latter towards the former when synchronisation happens. The sub-domain can be defined in either the physical space or the Fourier space (For exposition purpose, we call the velocity in this sub-domain the master modes). In nudging coupling, a

† Email address for correspondence: yili@sheffield.ac.uk

forcing term is introduced into either one or both of the two flows. The forcing term drives one flow towards the other (one-way coupling) or the two flows towards each other (two-way coupling). Though the interest in the topic sees resurgence recently, the earliest research can be traced back to two decades ago. Henshaw *et al.* (2003) investigates the synchronisation of turbulent flows, where a theoretical estimation is derived for the number of Fourier modes required to synchronise two solutions of both Burgers' equations and unforced Navier-Stokes equations (NSE). Numerical simulations are conducted to show the theoretical analysis tends to over estimate the bound. Soon after, Yoshida *et al.* (2005) investigate the complete synchronisation of two isotropic turbulent flows in three-dimensional (3D) periodic boxes and find that it is achieved if all Fourier modes with wavenumber less than at least  $k_c$  are used as the master modes, where  $k_c\eta \approx 0.2$  and  $\eta$  is the Kolmogorov length scale (see also Lalescu *et al.* (2013)). More recent work include the synchronisation of two direct numerical simulations (DNS) of isotropic turbulence using the nudging coupling (Di Leoni *et al.* 2020) and the investigation on partial synchronisation when the number of master modes is smaller than the threshold value, as is shown in Vela-Martin (2021). Nikolaidis & Ioannou (2022) investigates the synchronisation of Couette flows by coupling selected streamwise Fourier modes. They compute the conditional leading Lyapunov exponents (LLEs) (Boccaletti *et al.* 2002) and show that synchronisation happens when the exponent is negative. Channel flows are investigated by Wang & Zaki (2022) where the synchronisability of the flows using velocity from different spatial domains as the master modes is investigated. This work appears to be the first to investigate master-slave coupling in physical space. Inubushi *et al.* (2023) revisit the synchronisation of turbulence in a periodic box at Reynolds numbers higher than attempted before. Though they also find  $k_c\eta$  to be approximately 0.2 based on the results for the conditional LLEs (the transverse Lyapunov exponents in their terminology), it is noted that the conditional LLEs, hence the exact threshold value for  $k_c\eta$ , depend to some extent on the Reynolds number. The finding echoes what is noted in Boffetta & Musacchio (2017) and Berera & Ho (2018), that the non-dimensionalized LLE depends weakly on the Reynolds number. Wang *et al.* (2023) also investigate the cases when the large-scale data is not sufficient to dominate the small scales. Several techniques are employed to improve the correlation between the small scales when only partial synchronisation is achieved. Li *et al.* (2024) reports an investigation into the synchronisation of rotating turbulence in a 3D periodic box. They show that the forcing scheme and the rotation rate may have significant impacts on the threshold wavenumber. Interestingly, they find that the energy spectra of the leading Lyapunov vectors (LLVs) always seem to peak around  $k_c$ , suggesting a possible physical connection between the synchronisation threshold and the LLVs.

With regard to the synchronisation between LES and DNS, only two investigations appear to have been reported so far. Using nudging coupling, Buzzicotti & Leoni (2020) identify the optimal parameters in subgrid-scale (SGS) stress models that minimise the synchronisation error, which does not approach zero as LES does not converge to DNS exactly. Li *et al.* (2022) study the synchronisation between LES and DNS using the master-slave coupling, focusing on the threshold wavenumber and the behaviours of different SGS stress models. LES is an indispensable approach to model, and understand the physics of, high Reynolds number turbulent flows. Thus we believe that the synchronisation between LES and DNS is a topic that requires further research. Previous work leaves multiple interesting questions unanswered, among which we highlight three. Firstly, it is well-known that synchronisation is intrinsically related to the LLEs of the flows involved. However, even though the LLEs of LES have been calculated in several previous works (Nastac *et al.* 2017; Budanur & Kantz 2022), how they are related to those of DNS is not clear. This question should be addressed in order to better interpret the results for the LLEs of LES and their relationship to the synchronisation between LES and DNS.

Secondly, the threshold wavenumber for complete synchronisation between identical DNS is determined by the conditional LLEs of the flow (Boccaletti *et al.* 2002; Nikolaidis & Ioannou 2022; Wang & Zaki 2022). However, the synchronisation between LES and DNS occurs in a more general sense, where the master and the slave are mathematically different systems. How the threshold wavenumber for these systems is related to the conditional LLEs is not obvious. More broadly, how the conditional LLEs depend on the nature of the master system is also a question. We note that the latter question has not been raised before because it is irrelevant to the synchronisation of identical systems.

Thirdly, very recently, it has been found in rotating turbulence that the energy spectra of the LLVs appear to peak around the threshold wavenumber for synchronisation (Li *et al.* 2024). The observation potentially provides a new way to characterise the synchronisability of turbulent flows. It is thus of great interest to check if the same holds for the synchronisation of non-rotating turbulence, either between identical systems (e.g., between LES and LES, or between DNS and DNS), or between non-identical systems (e.g., between LES and DNS).

In this paper, we intend to address the above questions, and discuss how the results depend on the SGS stress models. The answers to these questions will add to our understanding of the synchronisation mechanism between turbulent flows. The paper is organised as follows. We introduce the governing equations in Section 2, and the details of the numerical experiments in Section 3. The results are presented and discussed in Sec. 4. Sec. 5 summarises the main conclusions.

## 2. Governing equations

### 2.1. Flow field simulations

We consider incompressible turbulent flows in a 3D periodic box  $[0, 2\pi]^3$ . The velocity fields are computed by either DNS or LES. DNS are conducted for flows with lower Reynolds numbers, where we integrate the Navier-Stokes equations (NSE)

$$\partial_t \mathbf{u} + (\mathbf{u} \cdot \nabla) \mathbf{u} = -\nabla p + \nu \nabla^2 \mathbf{u} + \mathbf{f}, \quad (2.1)$$

in which  $\mathbf{u} \equiv (u_1, u_2, u_3)$  is the velocity field,  $p$  is the pressure (divided by the constant density),  $\nu$  is the viscosity, and  $\mathbf{f}$  is the forcing term. The velocity is assumed to be incompressible so that

$$\nabla \cdot \mathbf{u} = 0. \quad (2.2)$$

LES are conducted by solving the filtered NSE (fNSE), given by

$$\partial_t \bar{\mathbf{u}} + (\bar{\mathbf{u}} \cdot \nabla) \bar{\mathbf{u}} = -\nabla \bar{p} + \nabla \cdot (-\boldsymbol{\tau}) + \nu \nabla^2 \bar{\mathbf{u}} + \bar{\mathbf{f}} + \mathbf{f}_s, \quad (2.3)$$

as well as the filtered continuity equation  $\nabla \cdot \bar{\mathbf{u}} = 0$ , where the over-line  $\bar{\cdot}$  represents filtering with filter length  $\Delta$ ,  $\bar{\mathbf{u}}$  and  $\bar{p}$  are the filtered velocity and pressure, respectively, and  $\boldsymbol{\tau}$  is the SGS stress tensor defined as

$$\boldsymbol{\tau}_{ij} = \bar{u}_i \bar{u}_j - \bar{u}_i \bar{u}_j.$$

Furthermore,  $\bar{\mathbf{f}}$  is the filtered forcing term, whereas  $\mathbf{f}_s$  symbolically represents the effects of coupling in synchronisation experiments, which will be further explained below.  $\mathbf{f}_s$  may be zero if the coupling does not affect the particular flow in consideration.

We use Kolmogorov forcing in all simulations, where  $\mathbf{f}$  is given by simple sinusoidal functions. Specifically, we let

$$\mathbf{f} \equiv (a_f \cos k_f x_2, 0, 0) \quad (2.4)$$

where  $a_f$  and  $k_f$  are constants chosen to be 0.15 and 1, respectively, in our simulations.

The flow resulting from this forcing is often called the Kolmogorov flow (Borue & Orszag 1996), and is inhomogeneous with a sinusoidal mean velocity profile. Previous research (Yoshida *et al.* 2005; Inubushi *et al.* 2023; Li *et al.* 2024) strongly suggests that the forcing only has at most secondary effects on the synchronisability of flows in periodic boxes for non-rotating turbulence. Therefore, though the forcing is different, the conclusions we draw can be compared with previous research.

As in Li *et al.* (2022), simulations with different SGS stress models are compared to highlight both the differences and commonalities of the results obtained with different models. The latter is particularly important in current research as it helps to demonstrate the universality of some observations, lending confidence in the applicability of the conclusions in real turbulence despite that they are obtained in LES. Three canonical models for  $\tau_{ij}$ , the standard Smagorinsky model, the dynamic Smagorinsky model, and the dynamic mixed model, are compared. For details of these models, see, e.g., Meneveau & Katz (2000). We summarise the formulae here for references. The standard Smagorinsky model (SSM) is defined with

$$\tau_{ij} = -2(c_s \Delta)^2 |\bar{s}| \bar{s}_{ij}, \quad (2.5)$$

where  $c_s = 0.16$  is the Smagorinsky coefficient,  $\bar{s}_{ij}$  is the filtered strain rate tensor given by

$$\bar{s}_{ij} = \frac{1}{2} (\partial_j \bar{u}_i + \partial_i \bar{u}_j), \quad (2.6)$$

and  $|\bar{s}| \equiv (2\bar{s}_{ij}\bar{s}_{ij})^{1/2}$  is the magnitude of the filtered strain rate. The dynamic Smagorinsky model (DSM) is also defined by Eq. (2.5), but the coefficient  $c_s^2$  is calculated dynamically using the Germano identity (Germano 1992). Following the procedure as described in, e.g., Germano (1992); Meneveau & Katz (2000), one can derive

$$c_s^2 = \frac{\langle L_{ij} M_{ij} \rangle_v}{\langle M_{ij} M_{ij} \rangle_v}, \quad (2.7)$$

with

$$M_{ij} = -2\Delta^2 \left[ 4|\tilde{s}|\tilde{s}_{ij} - \widetilde{|\bar{s}|\bar{s}_{ij}} \right], \quad L_{ij} = \widetilde{\bar{u}_i \bar{u}_j} - \widetilde{\bar{u}_i} \widetilde{\bar{u}_j}, \quad (2.8)$$

where  $\langle \rangle_v$  represents volume average, and  $\widetilde{\cdot}$  denotes test-filtering with filter scale  $2\Delta$  using the cut-off filter (Pope 2000).

The dynamic mixed model (DMM) is a combination of the Smagorinsky model and a nonlinear model. Mathematically, the model is defined by

$$\tau_{ij} = -2(c_s \Delta)^2 |\bar{s}| \bar{s}_{ij} + c_{nl} \Delta^2 \bar{A}_{ik} \bar{A}_{jk}, \quad (2.9)$$

where  $\bar{A}_{ij} \equiv \partial_j \bar{u}_i$  is the filtered velocity gradient and  $c_{nl}$  is the nonlinear coefficient which is to be determined dynamically. Following the dynamic procedure, the expressions for  $c_s^2$  and  $c_{nl}$  are found to be

$$c_s^2 = \frac{\langle L_{ij} M_{ij} \rangle_v \langle N_{ij} N_{ij} \rangle_v - \langle L_{ij} N_{ij} \rangle_v \langle M_{ij} N_{ij} \rangle_v}{\langle M_{ij} M_{ij} \rangle_v \langle N_{ij} N_{ij} \rangle_v - \langle M_{ij} N_{ij} \rangle_v^2}, \quad (2.10)$$

$$c_{nl} = \frac{\langle L_{ij} N_{ij} \rangle_v \langle M_{ij} M_{ij} \rangle_v - \langle L_{ij} M_{ij} \rangle_v \langle M_{ij} N_{ij} \rangle_v}{\langle M_{ij} M_{ij} \rangle_v \langle N_{ij} N_{ij} \rangle_v - \langle M_{ij} N_{ij} \rangle_v^2}, \quad (2.11)$$

where

$$N_{ij} = \Delta^2 \left[ 4\tilde{\bar{A}}_{ik} \tilde{\bar{A}}_{jk} - \widetilde{\bar{A}_{ik} \bar{A}_{jk}} \right]. \quad (2.12)$$

The three models are compared in depth in Kang *et al.* (2003) with experimental data obtained

in grid turbulence. DMM produces better agreement in most statistics and correlates better with the real SGS stress. SSM is known to be too dissipative. DSM has the same expression as SSM, but  $c_s^2$ , obtained dynamically, fluctuates slightly over time and in general is somewhat smaller. As a consequence, DSM is less dissipative compared with SSM, and in general, agrees with experimental data better than SSM.

## 2.2. The coupling between the masters and slaves

To answer the questions set out in the Introduction, we run two groups of synchronisation experiments, which are referred to as group I and group II, respectively. Group I consists of numerical experiments with lower Reynolds numbers so that we can compare the results with DNS data. Group II involves simulations with higher Reynolds numbers. These Reynolds numbers are not reachable by DNS given our limited resources. Therefore, only LES is involved in this group.

Two sets of synchronisation experiments are conducted in each group. In the first set, a master system  $M$  and two slave systems  $A$  and  $B$  are simulated concurrently.  $A$  and  $B$  are identical LES with the same SGS stress model.  $M$  is a DNS in Group I, whereas in Group II  $M$  is a LES with a SGS stress model different from the one in  $A$  and  $B$ . In the second set of experiments,  $A$  and  $B$  are coupled directly without system  $M$ , with  $A$  now serving as the master.

In the first set of experiments, system  $M$  and system  $A$  or  $B$  are different, therefore the synchronisation between  $M$  and  $A$  or between  $M$  and  $B$  is in a general sense. The setup for these experiments mimics the auxiliary-system method one uses to identify the synchronisation between non-identical systems (Boccaletti *et al.* 2002). The thesis is that, if  $A$  and  $B$  are eventually synchronised completely in this setup, then we may assert  $M$  and  $A$  are synchronised generally, in the sense that this shows there is a unique mapping between  $M$  and the slave (either  $A$  or  $B$ ). The experiments in this set are similar to those reported by Li *et al.* (2022), but here the analysis will centre around the properties of the conditional LLEs and the LLVs.

In the second set of experiments, complete synchronisation is possible between  $A$  and  $B$  as they are identical systems. These experiments are similar to those reported in, e.g., Inubushi *et al.* (2023); Li *et al.* (2024), in the sense that they all deal with synchronisation between identical systems. However, here the systems are filtered NSEs. The behaviours of the conditional LLEs, the LLVs, and their dependence on SGS stress models may display new features that do not exist in systems investigated previously.

The contrast between the two sets of experiments will illustrate the difference (or the lack thereof) between the two coupling methods: indirect coupling via a third (different) master system in the first set experiments versus direct coupling in the second set. The conjecture to be verified is that the synchronisability of the coupled systems is insensitive to the coupling mechanisms or the nature of the master system, at least when the master system is not too different from the slaves.

We now detail the coupling method in these experiments. Let  $\mathbf{u}_M(\mathbf{x}, t)$  be the velocity of system  $M$ , and  $\hat{\mathbf{u}}_M(\mathbf{k}, t)$  its Fourier mode, with  $\mathbf{k}$  being the wavenumber.  $\bar{\mathbf{u}}_A$  and  $\hat{\mathbf{u}}_A$ , and  $\bar{\mathbf{u}}_B$  and  $\hat{\mathbf{u}}_B$ , are defined similarly for systems  $A$  and  $B$ , respectively. More generally, hatted quantities are used to indicate Fourier transform. In the first set of experiments, system  $M$  is coupled to  $A$  and  $B$  via the master-slave coupling. Let  $k_m$  be a constant. In this coupling method, we overwrite the Fourier modes in  $\hat{\mathbf{u}}_A$  and  $\hat{\mathbf{u}}_B$  with  $|\mathbf{k}| \leq k_m$ , by those with same wavenumbers in  $\hat{\mathbf{u}}_M$  at each time step. That is,

$$\hat{\mathbf{u}}_A(\mathbf{k}, t) = \hat{\mathbf{u}}_B(\mathbf{k}, t) = \hat{\mathbf{u}}_M(\mathbf{k}, t), \quad (2.13)$$

for  $|\mathbf{k}| \leq k_m$ . Note that  $\mathbf{u}_M$  is a DNS velocity for the experiments in Group I, but an LES velocity for those in Group II.

The constant  $k_m$  is called the coupling wavenumber. The Fourier modes of these systems ( $M$ ,  $A$ , and  $B$ ) with  $|\mathbf{k}| \leq k_m$  are called the master modes whereas those with  $|\mathbf{k}| > k_m$  are called the slave modes. Systems  $A$  and  $B$  synchronise identically when  $k_m$  is sufficiently large (Li *et al.* 2022). The smallest  $k_m$  value for which such synchronisation happens is the threshold wavenumber, denoted as  $k_c$ .

In the second set of synchronisation experiments, systems  $A$  and  $B$  are coupled directly with  $A$  now serving as the master. The coupling is achieved by overwriting the Fourier modes in  $\hat{\mathbf{u}}_B(\mathbf{k}, t)$  with those in  $A$  for  $|\mathbf{k}| \leq k_m$ , so that

$$\hat{\mathbf{u}}_B(\mathbf{k}, t) = \hat{\mathbf{u}}_A(\mathbf{k}, t) \quad (2.14)$$

for  $|\mathbf{k}| \leq k_m$  at all time. Systems  $A$  and  $B$  are LES with the same SGS stress model so they are identical except for the initial states. We will compare the threshold wavenumbers  $k_c$  obtained in this set of experiments with those in the first set to illustrate the difference in the two coupling methods.

### 2.3. Lyapunov exponents and Lyapunov vectors

The synchronisation experiments are analysed via the LLEs (i.e., the leading Lyapunov exponents), the conditional LLEs, and the LLVs (i.e., the leading Lyapunov vectors) of the flows. There has been some limited work on the Lyapunov analysis of LES (Budanur & Kantz 2022; Nastac *et al.* 2017). However, to the best of our knowledge, there has not been an effort to look into the relationship between the LLEs of LES and those of DNS. The knowledge of the relationship, it appears to us, is required to interpret the results regarding the synchronisation of LES.

As will be shown later, the results strongly suggest that the LLE of a LES is a measure of the growth rate of low-pass filtered perturbation of a DNS of the same flow. Therefore, to discuss these results, we need to introduce the concept of LLEs of filtered DNS first. We consider unconditional LLEs only. Let  $\mathbf{u}$  be a DNS velocity, and  $\mathbf{u}_\Delta^\delta$  be the filtered infinitesimal perturbation, which is zero for wavenumber larger than the cut-off wavenumber  $k_\Delta \equiv \pi/\Delta$  where  $\Delta$  is the filter length. Mathematically, the Fourier mode of  $\mathbf{u}_\Delta^\delta$ , denoted by  $\hat{\mathbf{u}}_\Delta^\delta$ , satisfies

$$\hat{\mathbf{u}}_\Delta^\delta(\mathbf{k}, t) = 0 \quad (2.15)$$

for  $|\mathbf{k}| > k_\Delta$ . Also,  $\mathbf{u}_\Delta^\delta$  is divergence free and obeys the linearised NSE:

$$\partial_t \mathbf{u}_\Delta^\delta + (\mathbf{u} \cdot \nabla) \mathbf{u}_\Delta^\delta + (\mathbf{u}_\Delta^\delta \cdot \nabla) \mathbf{u} = -\nabla p^\delta + \nu \nabla^2 \mathbf{u}_\Delta^\delta + \mathbf{f}^\delta, \quad (2.16)$$

where  $p^\delta$  is the pressure perturbation and  $\mathbf{f}^\delta$  is the perturbation to the forcing term. The LLE for the filtered DNS, denoted by  $\lambda_\Delta$ , is defined as

$$\lambda_\Delta = \lim_{t \rightarrow \infty} \frac{1}{t} \log \frac{\|\mathbf{u}_\Delta^\delta(\mathbf{x}, t + t_0)\|}{\|\mathbf{u}_\Delta^\delta(\mathbf{x}, t_0)\|}, \quad (2.17)$$

where  $t_0$  is an arbitrary initial time whose choice does not affect the value of  $\lambda_\Delta$ , and  $\|\cdot\|$  represents the 2-norm defined by (for a generic vector field  $\mathbf{w}$ )

$$\|\mathbf{w}\| \equiv \langle \mathbf{w} \cdot \mathbf{w} \rangle_v^{1/2}. \quad (2.18)$$

Obviously  $\lambda_\Delta$  depends on the filter scale  $\Delta$ . It measures the average growth rate of the perturbations only applied to the Fourier modes of  $\mathbf{u}$  with length scales larger than  $\Delta$ .

Though in reality such perturbations are unlikely to be observed, we will show that  $\lambda_\Delta$  display similar behaviours as the LLEs of LES.

We now introduce the definition of the conditional LLE of a slave system in a synchronisation experiment, which describes the growth of infinitesimal perturbations to the slave modes. Let  $\bar{\mathbf{u}}$  be the LES velocity of a slave system in a simulation in either group I or group II, and  $\bar{\mathbf{u}}^\delta$  be an infinitesimal perturbation to *the slave modes* of  $\bar{\mathbf{u}}$ . As the master modes are not perturbed, we thus have

$$\hat{\bar{\mathbf{u}}}^\delta(\mathbf{k}, t) = 0 \quad \text{for} \quad |\mathbf{k}| \leq k_m. \quad (2.19)$$

The perturbation  $\bar{\mathbf{u}}^\delta$  obeys the linearised fNSE

$$\partial_t \bar{\mathbf{u}}^\delta + (\bar{\mathbf{u}} \cdot \nabla) \bar{\mathbf{u}}^\delta + (\bar{\mathbf{u}}^\delta \cdot \nabla) \bar{\mathbf{u}} = -\nabla \bar{p}^\delta + \nabla \cdot (-\boldsymbol{\tau}^\delta) + \nu \nabla^2 \bar{\mathbf{u}}^\delta + \bar{\mathbf{f}}^\delta, \quad (2.20)$$

and the continuity equation  $\nabla \cdot \bar{\mathbf{u}}^\delta = 0$ , where  $\bar{p}^\delta$ ,  $\bar{\mathbf{f}}^\delta$  and  $\boldsymbol{\tau}^\delta$  are the pressure perturbation, the perturbation to the filtered forcing, and the perturbation to the SGS stress  $\boldsymbol{\tau}$ , respectively.  $\bar{\mathbf{f}}^\delta$  is included for completeness, but it is actually always zero for the Kolmogorov forcing we are using.

The conditional LLE depends on  $k_m$ . Let it be  $\lambda(k_m)$ , then we have (Boccaletti *et al.* 2002; Nikolaidis & Ioannou 2022; Inubushi *et al.* 2023)

$$\lambda(k_m) = \lim_{t \rightarrow \infty} \frac{1}{t} \log \frac{\|\bar{\mathbf{u}}^\delta(\mathbf{x}, t + t_0)\|}{\|\bar{\mathbf{u}}^\delta(\mathbf{x}, t_0)\|}. \quad (2.21)$$

For  $k_m = 0$ ,  $\lambda(k_m)$  is the same as the usual (unconditional) LLE. The conditional LLE  $\lambda(k_m)$  measures the average growth rate of a perturbation to the *slave modes* of the slave system. For canonical low-dimensional chaotic systems such as the Lorenz system, synchronisation occurs only when the conditional LLE is negative (Boccaletti *et al.* 2002). The same behaviour is found for turbulent channel flows (Nikolaidis & Ioannou 2022), turbulence in periodic boxes (Inubushi *et al.* 2023), and rotating turbulence (Li *et al.* 2024). As a result, the threshold wavenumber  $k_c$  we mentioned previously is given by the equation  $\lambda(k_c) = 0$ . The questions we will address here are how the conditional LLEs depend on the SGS stress models and how they may differ for different coupling methods.

The conditional LLE is related to the growth rate of the kinetic energy of  $\bar{\mathbf{u}}^\delta$ , which is given by  $\|\bar{\mathbf{u}}^\delta\|^2/2$ . It follows readily from Eq. (2.20) that the rate of change of  $\|\bar{\mathbf{u}}^\delta\|^2/2$  is given by

$$\frac{d}{dt} \frac{\|\bar{\mathbf{u}}^\delta\|^2}{2} = \mathcal{P} - \mathcal{D} - \mathcal{T} + \mathcal{F}, \quad (2.22)$$

where

$$\mathcal{P} \equiv \langle -\bar{u}_i^\delta \bar{u}_j^\delta \bar{s}_{ij} \rangle_v, \quad \mathcal{D} \equiv \nu \langle \partial_j \bar{u}_i^\delta \partial_j \bar{u}_i^\delta \rangle_v, \quad \mathcal{T} \equiv \langle -\tau_{ij}^\delta \bar{s}_{ij}^\delta \rangle_v, \quad \mathcal{F} \equiv \langle \bar{f}_i^\delta \bar{u}_i^\delta \rangle_v, \quad (2.23)$$

which are the production term, the viscous dissipation term, the SGS dissipation term, and the forcing term, respectively, with  $\bar{s}_{ij}^\delta$  being the strain rate tensor for the velocity perturbation. Eq. (2.22) is similar to those that have been derived previously (see, e.g., Li *et al.* (2024); Nikolaidis & Ioannou (2022); Wang & Zaki (2022); Inubushi *et al.* (2023); Ge *et al.* (2023)), except for the additional SGS dissipation term  $\mathcal{T}$ . Eqs. (2.21) and (2.22) together show that

$$\lambda(k_m) = \lim_{t \rightarrow \infty} \frac{1}{t} \int_{t_0}^{t+t_0} \frac{\mathcal{P} - \mathcal{D} - \mathcal{T} + \mathcal{F}}{\|\bar{\mathbf{u}}^\delta\|^2} dt. \quad (2.24)$$

Therefore, the effects of SGS stress models on  $\lambda$  can be revealed from the analyses of  $\mathcal{P}$ ,  $\mathcal{D}$ , and  $\mathcal{T}$  (as we commented above,  $\mathcal{F} = 0$  in our simulations).

For sufficiently large  $t$  (strictly speaking, for  $t \rightarrow \infty$ ), the perturbation velocity  $\bar{u}^\delta$  approaches the leading backward Lyapunov vector (Bohr *et al.* 1998; Kuptsov & Parlitz 2012; Nikolay 2018). We will simply refer to it as the leading Lyapunov vector (LLV), if  $k_m = 0$ , or the conditional LLV, if  $k_m \neq 0$ . Like LLV, which is the most unstable perturbation to the velocity field in an average sense, the conditional LLV gives a measure for the most unstable perturbation to the slave modes in the velocity field. The interesting properties of the unconditional LLV for a turbulent channel flow are analysed in Nikolay (2018). In our previous work (Li *et al.* 2024), we find that the threshold coupling wavenumber  $k_c$  correlates closely with the peak of the averaged energy spectrum of the LLVs. Therefore, one of the objectives of this work is to look into the properties of the LLVs in relation to the synchronisability of LES.

### 3. The numerical experiments

#### 3.1. Summary of the numerical experiments

Tables 1 and 2 summarise the key parameters for the LES in Group I and II, respectively, with the definitions of the parameters given below in subsection 3.2. We label a case with a code that consists of three segments. The first segment starting from the left is in the form of ‘Ra’ with  $a$  being an integer between 1 and 5. Different  $a$  corresponds to different kinetic viscosity  $\nu$ . The middle segment is the acronym of the SGS stress model. The third segment is the value of  $N_{\text{LES}}$ , with  $N_{\text{LES}}^3$  being the number of grid points of the simulation. Each case (i.e., each code) represents a series of simulations with different coupling wavenumber  $k_m$ . Where necessary, we append ‘Kb’ to the end of the code to differentiate such simulations, where  $b$  is the value of  $k_m$ . Also, the cases with codes starting with the same ‘Ra’ are sometimes collectively referred to as ‘subgroup Ra’. The cases in such a subgroup may have different SGS stress models,  $N_{\text{LES}}$  or  $k_m$ .

The parameters for the DNSs corresponding to the LESs in Table 1 are summarised in Table 3. We use ‘RaDNS’ with  $N_{\text{DNS}}$  appended,  $N_{\text{DNS}}^3$  being the number of grid points for the simulation, to refer to the DNS in subgroup Ra. Note that each subgroup Ra is associated with at most a single DNS (there is no DNS for subgroups R4 and R5). In total, we conduct about 300 simulations where two or three velocity fields are solved concurrently (c.f. Section 3.3), with up to  $256^3$  grid points for each field.

#### 3.2. Definitions and values of key parameters

In this subsection, we summarise briefly the main parameters that characterise the simulations and normalise our results. Many parameters are calculated from the energy spectrum. Using  $\mathbf{v}(\mathbf{x}, t)$  and  $\hat{\mathbf{v}}(\mathbf{k}, t)$  to represent a generic DNS or LES velocity field and its Fourier transform, respectively, the energy spectrum of  $\mathbf{v}$  is denoted by  $E(k)$  with

$$E(k) = \frac{1}{2} \sum_{k \leq |\mathbf{k}| \leq k+1} \langle \hat{\mathbf{v}}(\mathbf{k}, t) \cdot \hat{\mathbf{v}}^*(\mathbf{k}, t) \rangle \quad (3.1)$$

where  $*$  denotes complex conjugate, and  $\langle \rangle$  represents ensemble average, i.e., average over space and time as well as different realisations where applicable.

The total turbulent kinetic energy  $K$  and the viscous energy dissipation rate  $\epsilon$  are both calculated from  $E(k)$  with

$$K = \int_0^\infty E(k) dk, \quad \epsilon = 2\nu \int_0^\infty k^2 E(k) dk. \quad (3.2)$$

Case	$Re_\lambda$	$\nu$	$\delta t$	$u_{\text{rms}}$	$\epsilon_t$	$\eta$	$\lambda_a$	$\tau_\Delta$	$\tau_k$	$\Delta_t$
R1SSM64	74	0.0060	0.0057	0.64	0.074	0.041	0.70	0.68	0.29	0.049
R1SSM96	73	0.0060	0.0057	0.62	0.071	0.042	0.70	0.52	0.29	0.046
R1DSM64	72	0.0060	0.0057	0.62	0.071	0.042	0.70	0.68	0.29	0.044
R1DSM96	73	0.0060	0.0057	0.62	0.070	0.042	0.70	0.52	0.29	0.043
R1DMM64	74	0.0060	0.0057	0.64	0.077	0.041	0.69	0.67	0.28	0.045
R1DMM96	73	0.0060	0.0057	0.63	0.073	0.041	0.70	0.51	0.29	0.043
R2SSM64	90	0.0044	0.0039	0.65	0.076	0.033	0.61	0.67	0.24	0.042
R2SSM128	86	0.0044	0.0039	0.62	0.071	0.033	0.60	0.43	0.25	0.036
R2DSM64	89	0.0044	0.0039	0.65	0.077	0.032	0.60	0.66	0.24	0.036
R2DSM128	89	0.0044	0.0039	0.64	0.074	0.033	0.61	0.42	0.24	0.033
R2DMM64	86	0.0044	0.0039	0.62	0.070	0.033	0.61	0.69	0.25	0.039
R2DMM128	87	0.0044	0.0039	0.64	0.077	0.032	0.59	0.42	0.24	0.033
R3SSM64	100	0.0030	0.0029	0.61	0.070	0.025	0.49	0.69	0.21	0.036
R3SSM128	115	0.0030	0.0029	0.68	0.079	0.024	0.51	0.41	0.20	0.028
R3DSM64	108	0.0030	0.0029	0.65	0.078	0.024	0.49	0.66	0.20	0.030
R3DSM128	109	0.0030	0.0029	0.66	0.077	0.024	0.50	0.42	0.20	0.025
R3DMM64	104	0.0030	0.0029	0.63	0.072	0.025	0.50	0.68	0.20	0.033
R3DMM128	107	0.0030	0.0029	0.65	0.076	0.024	0.50	0.42	0.20	0.026

Table 1: Parameters for lower Reynolds number LESs in Group I.

Case	$Re_\lambda$	$\nu$	$\delta t$	$u_{\text{rms}}$	$\epsilon_t$	$\eta$	$\lambda_a$	$\tau_\Delta$	$\tau_k$	$\Delta_t$
R4SSM32	401	0.0002	0.004	0.62	0.070	0.0033	0.13	1.10	0.053	0.045
R4SSM64	418	0.0002	0.004	0.65	0.076	0.0032	0.13	0.67	0.051	0.023
R4SSM128	459	0.0002	0.004	0.70	0.086	0.0031	0.13	0.40	0.048	0.012
R4SSM256	424	0.0002	0.004	0.64	0.071	0.0033	0.13	0.27	0.053	0.007
R4DSM32	420	0.0002	0.004	0.65	0.075	0.0032	0.13	1.08	0.052	0.037
R4DSM64	422	0.0002	0.004	0.64	0.070	0.0033	0.13	0.69	0.053	0.019
R4DSM128	450	0.0002	0.004	0.69	0.084	0.0031	0.13	0.40	0.049	0.010
R4DSM256	431	0.0002	0.004	0.66	0.077	0.0032	0.13	0.26	0.051	0.006
R4DMM32	443	0.0002	0.004	0.71	0.096	0.0030	0.13	1.00	0.046	0.049
R4DMM64	435	0.0002	0.004	0.65	0.073	0.0032	0.13	0.68	0.052	0.025
R4DMM128	414	0.0002	0.004	0.64	0.075	0.0032	0.13	0.42	0.051	0.013
R4DMM256	445	0.0002	0.004	0.67	0.078	0.0032	0.13	0.26	0.051	0.007
R5SSM32	569	0.0001	0.003	0.64	0.077	0.0019	0.09	1.07	0.036	0.045
R5SSM64	612	0.0001	0.003	0.66	0.076	0.0019	0.09	0.67	0.036	0.022
R5SSM128	663	0.0001	0.003	0.70	0.083	0.0019	0.09	0.41	0.035	0.011
R5SSM256	661	0.0001	0.003	0.70	0.081	0.0019	0.09	0.26	0.035	0.006
R5DSM32	627	0.0001	0.003	0.67	0.078	0.0019	0.09	1.07	0.036	0.037
R5DSM64	639	0.0001	0.003	0.67	0.075	0.0019	0.10	0.67	0.037	0.018
R5DSM128	648	0.0001	0.003	0.70	0.088	0.0018	0.09	0.40	0.034	0.009
R5DSM256	655	0.0001	0.003	0.70	0.083	0.0019	0.09	0.25	0.035	0.005
R5DMM32	570	0.0001	0.003	0.65	0.084	0.0019	0.09	1.04	0.034	0.050
R5DMM64	576	0.0001	0.003	0.65	0.078	0.0019	0.09	0.66	0.036	0.025
R5DMM128	572	0.0001	0.003	0.63	0.072	0.0019	0.09	0.43	0.037	0.012
R5DMM256	646	0.0001	0.003	0.70	0.087	0.0018	0.09	0.25	0.034	0.006

Table 2: Parameters for the high Reynolds number LESs in Group II.

Case	$N_{\text{DNS}}$	$Re_\lambda$	$u_{\text{rms}}$	$\epsilon$	$\eta$	$\nu$	$\lambda_a$	$\tau_k$
R1DNS128	128	75	0.63	0.072	0.042	0.0060	0.71	0.30
R2DNS192	192	90	0.65	0.074	0.033	0.0044	0.61	0.24
R3DNS256	256	112	0.66	0.077	0.024	0.0030	0.51	0.20

Table 3: Parameters for the DNSs corresponding to the LESs in subgroups R1, R2, and R3 in Group I.

The above equations apply to both LES and DNS, with the understanding that  $E(k) = 0$  when  $k \geq k_\Delta$  for LES.

For DNS velocity, the viscous energy dissipation rate  $\epsilon$  is one of the key parameters characterising small scale motions, by virtue of the fact that it equals the mean inter-scale energy flux in stationary turbulent flows (Pope 2000). If only the LES velocity of a flow is available, the inter-scale energy flux for the *underlying true velocity* has to be approximated, and it can be approximated by the sum of the viscous energy dissipation  $\epsilon$  and the SGS energy dissipation  $\Pi_\Delta \equiv -\langle \tau_{ij} \bar{s}_{ij} \rangle$  (Meneveau & Katz 2000; Pope 2000), both of which can be calculated from the LES velocity (with  $\tau_{ij}$  given by a SGS stress model). The sum is denoted by  $\epsilon_t$ , i.e.,

$$\epsilon_t = \epsilon + \Pi_\Delta = \epsilon - \langle \tau_{ij} \bar{s}_{ij} \rangle, \quad (3.3)$$

and will be called the total energy dissipation rate.

From  $\epsilon_t$  and  $K$ , we define the root-mean-square (RMS) velocity  $u_{\text{rms}}$ , the Taylor length scale  $\lambda_a$ , and the Taylor Reynolds number via

$$u_{\text{rms}} = (2K/3)^{1/2}, \quad \lambda_a = (15\nu u_{\text{rms}}^2 / \epsilon_t)^{1/2}, \quad Re_\lambda = \frac{u_{\text{rms}} \lambda_a}{\nu}. \quad (3.4)$$

Kolmogorov length scale  $\eta$  and time scale  $\tau_k$  are defined as

$$\eta = (\nu^3 / \epsilon_t)^{1/4}, \quad \tau_k = (\nu / \epsilon_t)^{1/2}. \quad (3.5)$$

For the DNS velocity fields, we replace  $\epsilon_t$  in Eqs. 3.4 and 3.5 by  $\epsilon$ , which then leads to the usual definitions. For LES, the parameters defined in Eqs. 3.4 and 3.5 have to be understood as approximations to those of the underlying true velocity for which the LES velocity is an approximation. It turns out that these parameters are useful for the characterisation of the results we will present later.

As one can see from Tables 1 and 3, for flows in Group I, the total dissipation  $\epsilon_t$  calculated from LES are only slightly different from  $\epsilon$  for the DNS of the same flow. For the simulations in Group II, we postulate that  $\epsilon_t$  is also close to the energy dissipation rate for the underlying true flows, although we do not have DNS data to verify the claim. For consistency, the LES results are always non-dimensionalised by the parameters defined with  $\epsilon_t$  as above, including those from Group I, even though DNS data are available for the cases in this group. The parameters defined with  $\epsilon$  are only calculated for the DNS and used to normalise the DNS results.

In addition, the eddy turnover time scale at the filter scale  $\Delta$ , denoted by  $\tau_\Delta$ , is defined as

$$\tau_\Delta = \Delta^{2/3} \epsilon_t^{-1/3}. \quad (3.6)$$

$\tau_\Delta$  is expected to be a suitable time scales to characterize the Lyapunov exponents in LES with high Reynolds numbers.

As will be shown later, it is also instructive to correlate the LES results (in particular the

threshold wavenumber  $k_c$ ) using an effective dissipation length scale  $\Delta_t$ . This length scale is defined in a way similar to how  $\eta$  is defined for DNS velocity. We firstly define an effective viscosity  $\nu_t$ , which is defined in such a way that the total energy dissipation can be modelled by an eddy viscosity model with the given effective viscosity. Mathematically, this means

$$\epsilon_t \equiv 2\nu_t \langle \bar{s}_{ij} \bar{s}_{ij} \rangle, \quad (3.7)$$

hence

$$\nu_t = \frac{\epsilon_t}{2\langle \bar{s}_{ij} \bar{s}_{ij} \rangle}. \quad (3.8)$$

Using  $\nu_t$  and  $\epsilon_t$ , the effective dissipation length scale  $\Delta_t$  is defined by

$$\Delta_t = (\nu_t^3 / \epsilon_t)^{1/4}. \quad (3.9)$$

Based on Kolmogorov phenomenology,  $\Delta_t$  should be linearly related to  $\Delta$  at high Reynolds numbers. However, as our numerical experiments will show later,  $\Delta_t$  provides better correlation with data than  $\Delta$ .

### 3.3. Numerical methods

Key information for the numerical schemes is given in what follows. The NSE and the fNSE (Eqs. (2.1) and (2.3)), together with the continuity and filtered continuity equations, are solved with the pseudo-spectral method in a periodic box  $V = [0, 2\pi]^3$ . The domain is discretised uniformly with  $N_{\text{DNS}}^3$  and  $N_{\text{LES}}^3$  grid points for DNS and LES, respectively. The two-thirds rule (Pope 2000) is used to remove the aliasing error in the advection term so that the maximum effective wavenumber is  $N_{\text{DNS}}/3$  for DNS and  $N_{\text{LES}}/3$  for LES. Time stepping uses an explicit second-order Euler scheme with a first-order predictor and a corrector based on the trapezoid rule (Li *et al.* 2020). The viscous diffusion term is treated with an integration factor before discretization in time is applied. The step-size  $\delta t$  is chosen in such a way that the Courant-Friedrichs-Lowy number  $u_{\text{rms}}\delta t/\delta x$  is less than 0.1, where  $\delta x$  is the grid size.

The conditional LLEs of a flow can be calculated in much the same way the traditional unconditional leading Lyapunov exponent is calculated, using the algorithm reported in, e.g., Boffetta & Musacchio (2017); Budanur & Kantz (2022). That is, one runs twin simulations concurrently, with velocity fields  $\bar{\mathbf{u}}_A$  and  $\bar{\mathbf{u}}_B$ , respectively. The two velocity fields initially differ by a small perturbation such that

$$e \equiv \|\bar{\mathbf{u}}_A(\mathbf{x}, 0) - \bar{\mathbf{u}}_B(\mathbf{x}, 0)\| \quad (3.10)$$

is a small value. The perturbation is only introduced to the Fourier modes with wavenumbers  $|\mathbf{k}| > k_m$ . In the first set of experiments (c.f. Section 2.2),  $\bar{\mathbf{u}}_A$  and  $\bar{\mathbf{u}}_B$  are coupled directly, as described previously. In the second set of experiments, they are coupled indirectly through a third master flow  $\mathbf{u}_M$ , which means  $\mathbf{u}_M$  is also integrated concurrently.  $\bar{\mathbf{u}}_B$  is periodically re-initialised at  $t_n = n\Delta t$  ( $n = 1, 2, \dots$ ) for some short time interval  $\Delta t$  (which is different from the step-size  $\delta t$ ). Specifically,  $\bar{\mathbf{u}}_B$  is re-initialised such that

$$\bar{\mathbf{u}}_B(\mathbf{x}, t_n^+) = \bar{\mathbf{u}}_A(\mathbf{x}, t_n) + g_n^{-1} [\bar{\mathbf{u}}_B(\mathbf{x}, t_n^-) - \bar{\mathbf{u}}_A(\mathbf{x}, t_n)], \quad (3.11)$$

where  $t_n^-$  and  $t_n^+$  represent times immediately before and after  $t_n$ , respectively, and

$$g_n = e^{-1} \|\bar{\mathbf{u}}_B(\mathbf{x}, t_n^-) - \bar{\mathbf{u}}_A(\mathbf{x}, t_n)\| \quad (3.12)$$

which is the factor by which the perturbation is amplified between  $t_{n-1}$  and  $t_n$ . By Eq. (3.11), the magnitude of the perturbation  $\bar{\mathbf{u}}_B - \bar{\mathbf{u}}_A$  is reduced to its initial value  $e$  after re-initialisation while the structure of the perturbation is unchanged. The conditional LLE is

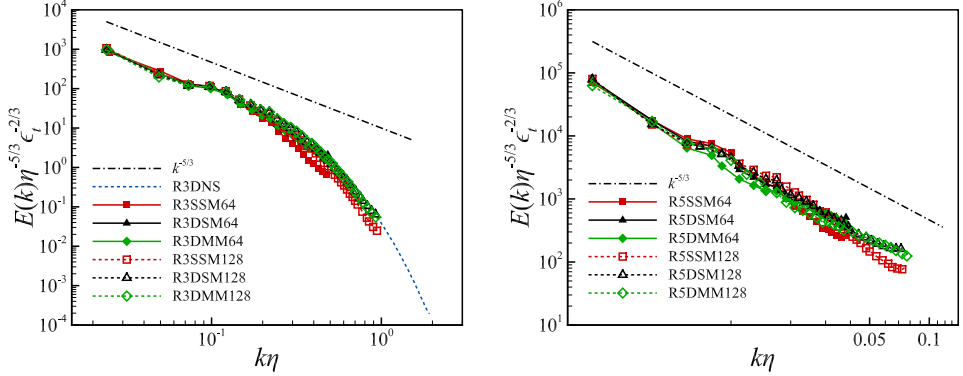


Figure 1: The energy spectra. Left: For cases in R3. Right: For cases in R5. Dash-dotted lines without symbols: the  $k^{-5/3}$  power law. Dashed lines without symbol: DNS for R3.

calculated from  $g_n$  by

$$\lambda(k_m) \approx \lim_{M \rightarrow \infty} \frac{1}{M \Delta t} \sum_{n=1}^M \log g_n. \quad (3.13)$$

In our computation,  $\Delta t \approx 0.1\tau_k$  for cases in group I. It varies somewhat for cases in group II but is always kept no more than  $0.05\tau_\Delta$ .

Note that, because of the coupling between  $A$  and  $B$  (c.f., Eqs. (2.13) and (2.14)), the perturbation  $\bar{\mathbf{u}}_B - \bar{\mathbf{u}}_A$  is always zero for Fourier modes with wavenumber  $|\mathbf{k}| \leq k_m$ , as required by the definition of conditional LLEs (c.f. Eq. (2.19)).

We remark that the conditional LLEs cannot be calculated by simply solving Eq. (2.20) because  $\bar{\mathbf{u}}^\delta$  grows exponentially so the solution diverges before a long enough time sequence can be obtained. On the other hand, one can calculate them using Eq. (2.24) as soon as  $\bar{\mathbf{u}}_A$  and  $\bar{\mathbf{u}}_B$  have been obtained as above, taking  $\bar{\mathbf{u}}_B - \bar{\mathbf{u}}_A$  as an approximation for  $\bar{\mathbf{u}}^\delta$ . This method is also used in selected cases to cross check the results for the conditional LLEs.

Finally, the LLE for filtered DNS, namely  $\lambda_\Delta$ , is calculated in much the same way. Here we run two uncoupled DNS for  $\mathbf{u}_A$  and  $\mathbf{u}_B$ , respectively, and, when  $\mathbf{u}_B$  is re-initialised, the perturbation in Fourier modes with  $|\mathbf{k}| > k_\Delta$  is set to zero by letting

$$\hat{\mathbf{u}}_B(\mathbf{k}, t) = \hat{\mathbf{u}}_A(\mathbf{k}, t) \quad (|\mathbf{k}| > k_\Delta), \quad (3.14)$$

hence removing the perturbation to the Fourier modes with wavenumber beyond the cut-off wavenumber.

## 4. Results and analyses

### 4.1. Energy spectra

The simulations are validated using the energy spectra for selected cases. Fig. 1 shows the time-averaged energy spectra normalised by Kolmogorov parameters. The energy spectra shown in the left panel of Fig. 1 are from cases in subgroup R3, including one from the DNS. The DNS spectrum displays features that are consistent with the  $k^{-5/3}$  Kolmogorov spectrum. LES results are shown for two  $N_{LES}$  values. The features of the DNS spectrum are broadly captured by LES. For both  $N_{LES}$ , DSM and DMM reproduce the DNS spectrum quite closely, due to their ability to adjust the model coefficients dynamically. SSM slightly underestimates the high wavenumber end of the spectrum. The spectra for  $N_{LES} = 128$  (shown in empty symbols and dashed lines) are slightly more accurate than the ones for  $N_{LES} = 64$ . The

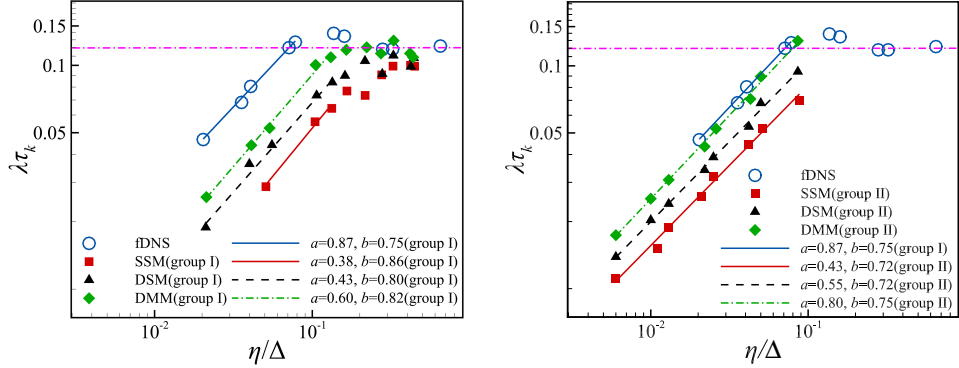


Figure 2: Normalised unconditional LLEs  $\lambda\tau_k$  as functions of  $\eta/\Delta$  for the cases in Group I (the left panel) and Group II (the right panel). The horizontal dash-dotted line indicates  $\lambda\tau_k = 0.12$  corresponding to the value for DNS with moderate Reynolds number (Boffetta & Musacchio 2017; Berera & Ho 2018; Inubushi *et al.* 2023).

results for the simulations in subgroup R5 are shown in the right panel of Fig. 1. Due to the higher  $Re_\lambda$ , no DNS results are available for comparison. However, an extended range with a slope of  $-5/3$  is clearly visible in the spectra, reproducing the expected feature of canonical turbulent flows. Again, the differences between the three models are in line with the literature. We highlight one observation, which is that DSM slightly overestimates the energy spectrum at the highest wavenumber end, whereas the spectrum calculated with DMM is free from this flaw. Same observation can be found in e.g. Kang *et al.* (2003); see Fig. 12 therein. This difference between DSM and DMM seems to be responsible for some observations we will discuss below.

#### 4.2. Unconditional leading Lyapunov exponents

##### 4.2.1. Relationship between the unconditional LLEs for LES and filtered DNS

In this subsection we focus on the results for the unconditional LLEs for LES, i.e.,  $\lambda(k_m = 0)$ . They are compared with the LLEs for filtered DNS,  $\lambda_\Delta$ . As we will show, our results are consistent with previous research (Nastac *et al.* 2017; Budanur & Kantz 2022), but the LLEs for filtered DNS appear to have not been reported before and we will reveal new behaviours with regard to the LLEs of the LES. These results provide a reference point for the discussion on the conditional LLEs. In this subsection we will simply use  $\lambda$  to represent  $\lambda(k_m = 0)$ .

The first results for the unconditional LLEs are shown in Fig. 2. The LLEs for all the cases in group I are plotted in the left panel, whereas those for group II are in the right panel. The results for LES are shown with solid symbols, which are to be compared with the LLEs for filtered DNS,  $\lambda_\Delta$ , shown with empty circles. The LLEs are normalised with the Kolmogorov parameters given in Tables 1 – 3. Note that these data include simulations with different Reynolds numbers.

In order to compare qualitatively with the results shown in Fig. 1 of Budanur & Kantz (2022) and Fig. 7 of Nastac *et al.* (2017), we have plotted  $\lambda\tau_k$  against  $\eta/\Delta$ . Other possible normalisations are discussed below. We start with the results for SSM in the left panel, because SSM is the only model considered in Budanur & Kantz (2022). Our results reproduce the trends shown in this previous work, in that  $\lambda\tau_k$  generally increases with  $\eta/\Delta$ . No clear scaling law is observed for large  $\eta/\Delta$ , but for smaller  $\eta/\Delta$ , it appears that the data can be fitted with a power-law. We will discuss the scaling behaviour in more details below after reviewing the results for other models.

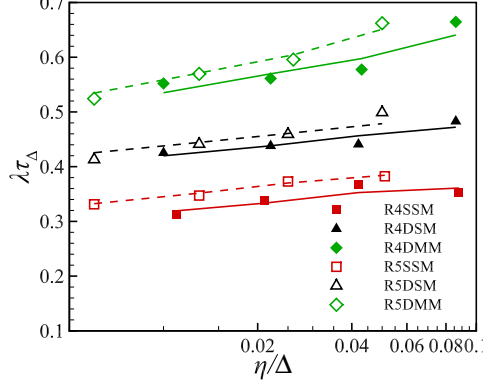


Figure 3: Normalised unconditional LLE  $\lambda\tau_\Delta$  as functions of  $\eta/\Delta$  for cases in subgroups R4 and R5.

The results for SSM can be compared with those for DSM, DMM and filtered DNS. In all cases, a scaling law emerges for small  $\eta/\Delta$ . For the three models, the scaling law emerges at a value of  $\eta/\Delta$  between 0.1 and 0.2. For filtered DNS, it emerges at around  $\eta/\Delta \sim 0.08$ . However, some general trends are observable across all values of  $\eta/\Delta$ . First of all, the LLEs obtained from LES with all three models are smaller than those obtained from filtered DNS. DMM leads to values closest to the latter, especially for  $\eta/\Delta$  larger than  $\sim 0.1$ , but the discrepancy is significant for smaller  $\eta/\Delta$ . The results for SSM displays the largest difference with filtered DNS, while DSM falls somewhere in between SSM and DMM.

The behaviours of SSM and DSM, arguably, can be attributed to the fact that both SSM and DSM are purely dissipative, and SSM is known to overestimate the dissipation. The behaviour of DMM is also consistent with the fact that DMM is generally more accurate.

The right panel of Fig. 2 plots the LES results for the cases in group II. These results correspond to higher Reynolds numbers with  $\eta/\Delta$  ranging from 0.006 to 0.1. The results display a clear scaling law over the whole range of values for  $\eta/\Delta$ . The values of the LLE are again largest for DMM and smallest for SSM. As we do not have DNS results at high Reynolds numbers, we reproduce in the right panel the results for filtered DNS already shown in the left panel, as a reference for the scaling behaviour. Not surprisingly, the results for LES follow approximately the same scaling behaviour displayed by the filtered DNS data.

We now discuss the scaling behaviours more quantitatively. A scaling law  $\lambda \sim \Delta^{-\rho}$  is proposed by Budanur & Kantz (2022) for the LLE calculated with SSM as the model. Based on data for  $0.05 < \eta/\Delta < 0.3$  at several different Reynolds numbers, it is found that  $\rho \approx 0.32$  gives a reasonable fit for the data. The value of 0.32 does not seem to be related to any known physical constants. Our data in Fig. 2, however, do not exhibit clear scaling behaviours for  $\eta/\Delta$  in the same range. Rather, the data strongly suggest that a more robust scaling law exists for smaller  $\eta/\Delta$ , and over a wider range. This scaling law appears to be more universal, being followed approximately by the data from all three models at different Reynolds numbers as well as the filtered DNS data. To quantify this scaling regime, a power-law in the form of

$$\lambda\tau_k = a(\eta/\Delta)^b \quad (4.1)$$

is used to fit the data. These functions are shown with lines in Fig. 2, for  $a$  and  $b$  obtained from linear regression for the transformed data  $(\ln \eta/\Delta, \ln \lambda\tau_k)$ . As shown in the figure, for the data in the left panel, the best fit is found with  $b \approx 0.86$  for SSM,  $b \approx 0.80$  for DSM, and  $b \approx 0.82$  for DMM. These values are slightly larger than the value  $b \approx 0.75$  for filtered DNS. For the data in the right panel,  $b \approx 0.72$  is found for both SSM and DSM and  $b \approx 0.75$

Coefficients	SSM	DSM	DMM
$(\alpha, \beta, c_1)$	$(0.05, 0.21, 0.12)$	$(0.05, 0.10, 0.29)$	$(0.08, 0.16, 0.29)$

Table 4: Coefficients for the fitting function of the data in Fig. 3 (c.f., Eq. (4.4)).

for DMM. Therefore, the exponents for the LES for all three SGS stress models only differ slightly from those of the filtered DNS, which we find to be interesting.

We note that the coefficient  $a$  is different numerically between LES and filtered DNS. However, the close agreement in the scaling exponent  $b$  strongly suggests that the LLEs for LES can be interpreted as approximations to the LLEs for filtered DNS at same filter scale  $\Delta$ . That is, the LLEs for LES are a measure of the growth rate of the low-pass filtered infinitesimal perturbations one would find in a DNS. This relationship between the LLEs of LES and filtered DNS, as intuitive as it may seem, has not been reported before.

#### 4.2.2. Scaling law and intermittency corrections

The discussion so far focuses on  $\lambda\tau_k$ . That is, the LLEs are normalised by  $\tau_k$ , following the method in the literature (Nastac *et al.* 2017; Budanur & Kantz 2022). However, dimensionally the most relevant time scale at the smallest scales of LES is  $\tau_\Delta$ . In fact, according to Kolmogorov phenomenology one may conjecture that

$$\lambda \sim \tau_\Delta^{-1}, \quad \lambda_\Delta \sim \tau_\Delta^{-1}, \quad (4.2)$$

so that  $\lambda\tau_\Delta$  is actually a constant. We explore this question further with the high Reynolds number simulations in Group II, as the scaling relations are expected to be more accurate at large Reynolds numbers. Using Eq. (4.1), it is easy to show that

$$\lambda\tau_\Delta = a \left( \frac{\eta}{\Delta} \right)^\alpha, \quad \alpha = b - \frac{2}{3}. \quad (4.3)$$

Based on the values of  $b$  we obtained previously (c.f., the right panel of Fig. 2), we find  $\alpha = 0.08$  for the filtered DNS data (obtained at lower Reynolds numbers),  $\alpha = 0.05$  for SSM and DSM, and  $\alpha = 0.08$  for DMM. Though these values are not exactly zero, we may nevertheless conclude that the scaling follows Kolmogorov phenomenology with some small corrections. We plot  $\lambda\tau_\Delta$  in Fig. 3, as a function of  $\eta/\Delta$  for the high Reynolds number data in group II. The data, shown with symbols, indeed display much weaker dependence on  $\eta/\Delta$ , as expected.

It is interesting to look into the corrections more quantitatively. Moreover, Fig. 3 also shows that, compared with  $\lambda\tau_k$ ,  $\lambda\tau_\Delta$  depends more strongly on the Reynolds number. For  $\lambda\tau_k$ , the data for different Reynolds numbers essentially collapse on the same curve (c.f., Fig. 2). However, in Fig. 3, there seems to be a systematic difference between results for subgroups R4 and R5 (which consequently have been plotted separately with solid and empty symbols, respectively). Therefore, the parameter  $a$  in Eq. (4.3) should depend on the Reynolds number, and we may write empirically

$$\lambda\tau_\Delta = c_1 \left( \frac{\eta}{\Delta} \right)^\alpha Re_\lambda^\beta, \quad (4.4)$$

for some constants  $c_1$  and  $\beta$ . The values for  $c_1$  and  $\beta$  are found with linear regression using the data indicated by the symbols in Fig. 3, and are documented in Table 4. Eq. (4.4) with coefficients given in Table 4 is shown with solid and dashed lines in Fig. 3. Table 4 shows

that the Reynolds-number dependence is mild with  $\beta$  ranging between 0.10 and 0.21 for the three SGS stress models.

To compare the above scaling relation with the literature, we rewrite Eq. (4.4) in terms of the Reynolds number defined with the integral length scale,  $L \equiv u_{\text{rms}}^3/\epsilon_t$ . It is easy to show that Eq. (4.4) implies

$$\lambda\tau_\Delta \sim Re_\lambda^{\beta-3\alpha/2} \left(\frac{\Delta}{L}\right)^{-\alpha} \sim Re_L^{\beta/2-3\alpha/4} \left(\frac{\Delta}{L}\right)^{-\alpha}, \quad (4.5)$$

where  $Re_L \equiv u_{\text{rms}}L/\nu$  is the integral scale Reynolds number which is related to  $Re_\lambda$  via  $Re_L \sim Re_\lambda^2$ . With the values of  $\alpha$  and  $\beta$  obtained above, we find

$$\lambda\tau_\Delta \sim \begin{cases} Re_L^{0.06} \left(\frac{\Delta}{L}\right)^{-0.05} & \text{for SSM,} \\ Re_L^{0.01} \left(\frac{\Delta}{L}\right)^{-0.05} & \text{for DSM,} \\ Re_L^{0.02} \left(\frac{\Delta}{L}\right)^{-0.08} & \text{for DMM.} \end{cases} \quad (4.6)$$

Therefore,  $\lambda\tau_\Delta$  increases with the Reynolds number, and also increases when  $\Delta/L$  is decreased. Both are corrections to the Kolmogorov scaling. As one may see, they are both relatively small, not unexpected.

The corrections are reminiscent of what is observed for the Lyapunov exponents of unfiltered DNS (Boffetta & Musacchio 2017; Berera & Ho 2018), where small deviation from Kolmogorov scaling is also found. The quantity corresponding to  $\lambda\tau_\Delta$  in those investigations is  $\lambda_{\text{DNS}}\tau_k$ , where  $\lambda_{\text{DNS}}$  represents the LLE for the unfiltered DNS. It has been found in, e.g., Boffetta & Musacchio (2017); Berera & Ho (2018), that  $\lambda_{\text{DNS}}\tau_k \sim Re_L^{0.14}$ , whereas the dimensional argument based on Kolmogorov phenomenology suggests  $\lambda_{\text{DNS}}\tau_k$  should be independent of the Reynolds number. The deviation is attributed to small-scale intermittency which is not accounted for in dimensional arguments (for reviews of small scale intermittency in turbulence, see, e.g. Frisch (1995); Sreenivasan & Antonia (1997)). The explanation also applies to our results, as the intermittency correction is expected to increase with the Reynolds number in LES in a similar way as in DNS. Meanwhile, because intermittency is stronger for smaller filter scale  $\Delta$ , the intermittency correction should be larger when  $\Delta/L$  is smaller. This is consistent with Eq. (4.6).

We note that Ge *et al.* (2023) recently proposed that the ‘sweeping’ effect could also be the cause of the correction. If the sweep effect is relevant, we should introduce the sweeping time scale  $u_{\text{rms}}/\eta$  (also known as the Eulerian time scale) into the parametrisation of  $\lambda_{\text{DNS}}\tau_k$ . As a result, different scaling relations with the Reynolds number may be obtained. However, it seems that the contribution of the sweeping time scale is still unclear, so we do not follow this line of inquiry any further.

Finally, it is also tempting to compare the results with the finite size Lyapunov exponents (FSLEs) analysed in, e.g., Boffetta *et al.* (2002); Boffetta & Musacchio (2017). The FSLE measures the growth rate of a finite size velocity perturbation  $\delta v$  by calculating the doubling time of the perturbation. It is found that the FSLE is  $\sim (\delta v)^{-2}$  in isotropic turbulence for  $\delta v$  corresponding to fluctuations over length scales in the inertial range. There is significant difference between the LLEs of an LES velocity field and the FSLE of a DNS velocity, as the LLEs measures the growth of infinitesimal velocity perturbation. Nevertheless, if we assume that the most unstable velocity perturbation scales with  $\Delta$  according to Kolmogorov scaling, we have  $\|\bar{u}^\delta\| \sim \Delta^{1/3}$ . Ignoring the intermittency corrections in Eq. (4.6), we thus have

$\lambda \sim \tau_\Delta^{-1}$ , hence

$$\lambda \sim \tau_\Delta^{-1} \sim \frac{\|\bar{\mathbf{u}}^\delta\|}{\Delta} \sim \|\bar{\mathbf{u}}^\delta\|^{-2}, \quad (4.7)$$

which mimics the scaling law for the FSLEs.

#### 4.2.3. The dynamics of the perturbations

To understand the results for  $\lambda\tau_\Delta$ , it is helpful to look into the dynamics of the perturbations, described by Eqs. 2.22 and 2.24, which show that the LLEs are the outcome of the interaction between the production, the dissipation, and SGS effects. These equations may shed light on the origin of the differences in the results between the SGS stress models. They might also offer insights on the deviation of the scaling relations from the Kolmogorov theory. Therefore in this subsection we look into the statistics of the key terms in Eqs. 2.22 and 2.24. We use

$$P \equiv \left\langle \frac{\mathcal{P}\tau_\Delta}{\|\bar{\mathbf{u}}^\delta\|^2} \right\rangle, \quad D \equiv \left\langle \frac{\mathcal{D}\tau_\Delta}{\|\bar{\mathbf{u}}^\delta\|^2} \right\rangle, \quad T \equiv \left\langle \frac{\mathcal{T}\tau_\Delta}{\|\bar{\mathbf{u}}^\delta\|^2} \right\rangle \quad (4.8)$$

to denote the averaged non-dimensionalised production, viscous dissipation and SGS dissipation terms, respectively. Per Eq. (2.24), we have

$$\lambda\tau_\Delta = P - D - T. \quad (4.9)$$

Note that the contribution from the forcing term is always zero, and that the time average has been replaced by ensemble average  $\langle \rangle$  which in practice includes both time average and average over multiple simulations. We will focus on the high Reynolds number simulations in Group II, which include subgroups R4 and R5 with the latter having higher Reynolds numbers than the former.

Fig. 4 shows the production term  $P$  (top-left panel), molecular dissipation  $D$  (top-right panel), SGS dissipation  $T$  (bottom-left panel) and  $D + T$  (bottom-right panel). The top-left panel shows that the production term  $P$  generally increase with  $Re_\lambda$  and  $\eta/\Delta$  for all three models. Those for DSM and DMM are close to each other, though the former seems to be slightly larger than the latter in general. Both are larger than that of SSM.

The difference in  $P$  between the models is likely a consequence of the difference in the energy spectra at the high wavenumber end (c.f. Fig. 1). The definition of  $P$  shows that larger strain rate tends to lead to larger  $P$ , and the magnitude of the strain rate is dominantly determined by the shape of the energy spectrum at high wavenumbers. As DSM leads to a slightly higher energy spectrum around the cut-off wavenumber compared with that of DMM, this will contribute to a higher production  $P$ . Meanwhile, the energy spectrum calculated with SSM is the lowest at the high wavenumber end. This also partly leads to a lower  $P$ .

The dissipation  $D$  (top-right panel) also increases with  $\eta/\Delta$  for all models, but does not depend on  $Re_\lambda$ . The results for DSM and DMM are essentially the same. For SSM,  $D$  is slightly smaller for larger  $\eta/\Delta$ , which is a likely due to the underestimated energy spectrum near the cut-off scale.

The SGS dissipation term  $T$  decreases mildly as  $\eta/\Delta$  increases, as shown in the bottom-left panel of Fig. 4. The trend is observed for all three models. For higher  $\eta/\Delta$ , where  $\Delta$  approaches  $\eta$ ,  $T$  is slightly smaller for larger  $Re_\lambda$ . For smaller  $\eta/\Delta$ , the dependence on  $Re_\lambda$  disappears, which is to be expected as the effects of molecular viscosity should become negligible when  $\Delta$  is much larger than  $\eta$ . The values of  $T$  for DSM are slightly lower than those for SSM, and both are significantly larger than those for DMM. In fact, the values for SSM and DSM are almost twice as large for small  $\eta/\Delta$ , and are about three times as large for large  $\eta/\Delta$ . The difference across the models for a large part comes from the difference in the magnitude of perturbation to the SGS stress,  $\tau_{ij}^\delta$ . For instance,  $c_s^2$  is on average approximately

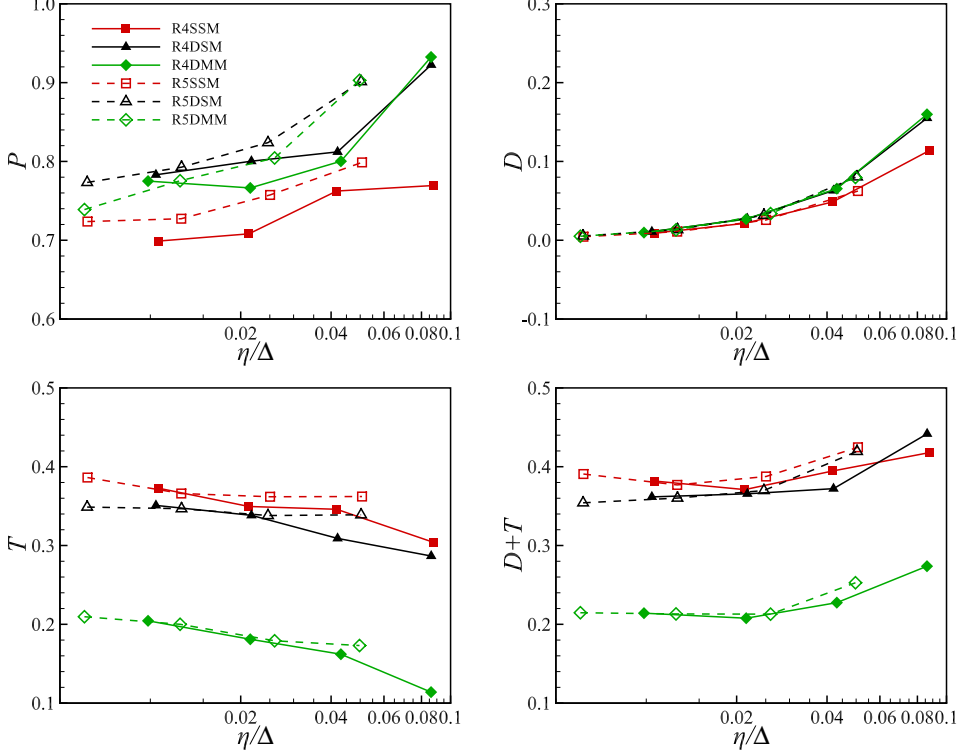


Figure 4: The production term  $P$  (top-left), viscous dissipation term  $D$  (top-right), SGS dissipation term  $T$  (bottom-left) and  $D+T$  (bottom-right) as functions of  $\eta/\Delta$  for cases in subgroups R4 and R5. Solid lines with solid symbols: R4. Dashed lines with empty symbols: R5. Squares: SSM. Deltas: DSM. Diamonds: DMM

0.018 for DSM in case R5DSM32, which is smaller than the value  $c_s^2 = 0.026$  for SSM. For DMM,  $c_s^2 \approx 0.013$  which is even smaller. Besides, by calculating the contributions of the eddy viscosity term and the nonlinear term in DMM separately, we can show that the latter makes negative contributions to  $T$  (figure omitted), which further reduces the value of  $T$  for DMM.

Since the difference in the viscous dissipation term  $D$  between the three models is small for high  $Re_\lambda$  (c.f., top-right panel of Fig. 4), the difference in  $\lambda\tau_\Delta$  between the models shown in Fig. 3 mainly comes from  $P$  and  $T$ , and especially from  $T$ . SSM has the smallest  $\lambda\tau_\Delta$  because it has the smallest  $P$  and largest  $T$  (c.f., Eq. (4.9)). For DSM, the production term  $P$  is very slightly larger compared with DMM. However, the SGS dissipation  $T$  for DSM is much larger. As a result, the LLE  $\lambda\tau_\Delta$  calculated with DSM is smaller compared with DMM.

The above discussion is concentrated on the difference between the three models. We now look into the dependence of  $\lambda\tau_\Delta$  on Reynolds number and  $\eta/\Delta$ . Despite the differences between the models, their production term  $P$  displays similar dependence on  $\eta/\Delta$  and  $Re_\lambda$ . That is, it always increases with the two. The sum  $D+T$  (bottom-right panel of Fig. 4) also increases with  $\eta/\Delta$  but shows no clear dependence on  $Re_\lambda$  when  $\eta/\Delta$  is small. Therefore,  $P$  shares the same behaviours that  $\lambda\tau_\Delta$  has shown in Fig. 3, where it increases with  $Re_\lambda$  and  $\eta/\Delta$ . Accordingly, we can understand the behaviours of  $\lambda\tau_\Delta$  through  $P$ . Though  $D+T$  shows similar dependence on  $\eta/\Delta$ , that precisely makes it a counteracting factor, according to Eq.

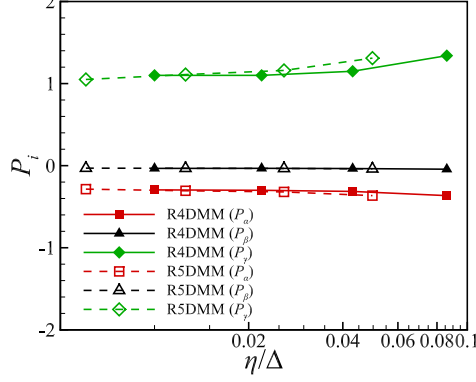


Figure 5: The components  $P_\alpha$ ,  $P_\beta$  and  $P_\gamma$  of the production term.

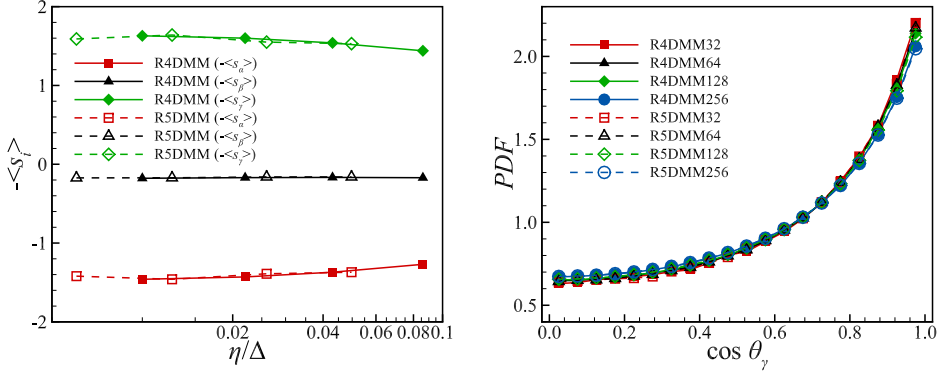


Figure 6: Left: (minus) mean eigenvalues  $-\langle s_\alpha \rangle$ ,  $-\langle s_\beta \rangle$ , and  $-\langle s_\gamma \rangle$ . Right: PDFs of  $\cos \theta_\gamma$ .

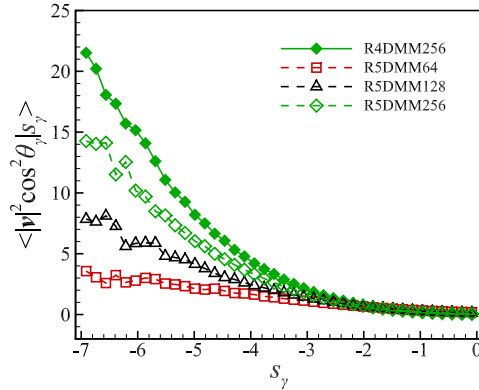


Figure 7: The conditional average  $\langle |\bar{v}|^2 \cos^2 \theta_\gamma | s_\gamma \rangle$ .

(4.9). Therefore, We now look into  $P$  to gain some understanding on the dynamical origin of  $\lambda \tau_\Delta$ 's behaviours. As all three models follow the same trends, we consider DMM only.

We start with the alignment between  $\bar{u}^\delta$  and  $\bar{s}_{ij}$ , and the statistics of the eigenvalues of  $\bar{s}_{ij}$ . Let  $\bar{s}_{ij}^+ \equiv \tau_\Delta \bar{s}_{ij}$  represent the dimensionless strain rate tensor, and  $\bar{v} = \bar{u}^\delta / \|\bar{u}^\delta\|$ , so

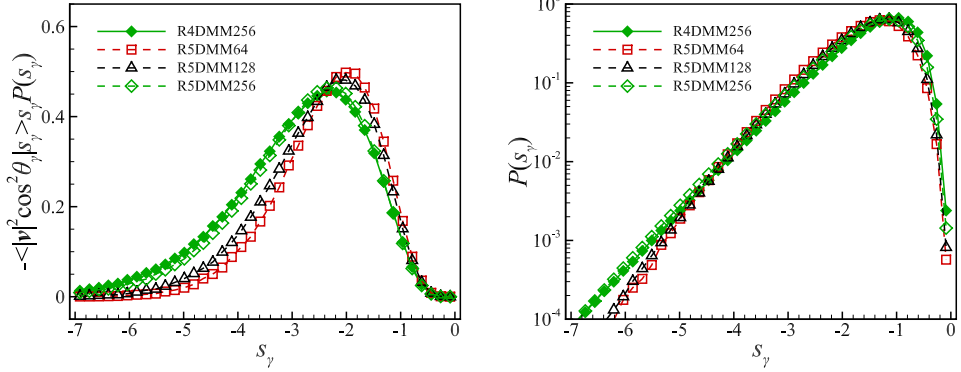


Figure 8: Left: weighted conditional average  $-\langle |\bar{v}|^2 \cos^2 \theta_\gamma |s_\gamma \rangle s_\gamma P(s_\gamma)$ . Right: PDF  $P(s_\gamma)$  of  $s_\gamma$ .

that  $P = -\langle \bar{v}_i \bar{v}_j \bar{s}_{ij}^+ \rangle$ . We let  $s_\alpha \geq s_\beta \geq s_\gamma$  be the eigenvalues of  $\bar{s}_{ij}^+$ , with corresponding eigenvectors  $e_i$  ( $i = \alpha, \beta, \gamma$ ). Due to incompressibility, we have  $s_\alpha + s_\beta + s_\gamma = 0$  and, as a result,  $s_\alpha \geq 0$  and  $s_\gamma \leq 0$ . Letting  $\theta_i$  be the angle between  $e_i$  and  $\bar{v}$ , we may write

$$P = P_\alpha + P_\beta + P_\gamma, \quad (4.10)$$

with

$$P_\alpha = -\langle s_\alpha |\bar{v}|^2 \cos^2 \theta_\alpha \rangle, P_\beta = -\langle s_\beta |\bar{v}|^2 \cos^2 \theta_\beta \rangle, P_\gamma = -\langle s_\gamma |\bar{v}|^2 \cos^2 \theta_\gamma \rangle, \quad (4.11)$$

where  $|\bar{v}|^2 \equiv \bar{v} \cdot \bar{v}$ . By virtue of the signs of  $s_\alpha$  and  $s_\gamma$ , we have  $P_\alpha \leq 0$  and  $P_\gamma \geq 0$ . Eq. (4.11) shows that the eigenvalues of  $\bar{s}_{ij}^+$  as well as the alignment between  $\bar{u}^\delta$  and the eigenvectors of  $\bar{s}_{ij}^+$  are useful to gain insights into  $P$ .

Fig. 5 shows  $P_\alpha$ ,  $P_\beta$  and  $P_\gamma$  as functions of  $\eta/\Delta$  for DMM for the cases in subgroups R4 and R5. The main observation is that the dominant term is  $P_\gamma$ . More importantly,  $P_\alpha$  and  $P_\beta$  are essentially independent of  $\eta/\Delta$ . Only  $P_\gamma$  increases with both  $Re_\lambda$  and  $\eta/\Delta$ , which thus must be the source of the same behaviours observed in  $P$ .

The behaviour of  $P_\gamma$ , interestingly, cannot be explained by the behaviours of the mean eigenvalue  $-\langle s_\gamma \rangle$  or  $\cos \theta_\gamma$  separately.  $-\langle s_\gamma \rangle$  (among others) is plotted in the left panel of Fig. 6, which shows that it decreases as  $\eta/\Delta$  increases, opposing the behaviour of  $P_\gamma$ . The PDFs of  $\cos \theta_\gamma$ , shown in the right panel of Fig. 6, display a strong peak at 1, the upper bound of  $|\cos \theta_\gamma|$ , which means that  $\bar{v}$  tends to align with  $e_\gamma$ . This trend contributes to the dominance of  $P_\gamma$  over  $P_\beta$  and  $P_\alpha$ , but the PDFs do not change appreciably with  $\eta/\Delta$ , hence failing to explain the increase in  $P_\gamma$  when  $\eta/\Delta$  increases. Therefore, the behaviour of  $P_\gamma$  has to be explained by the correlation between  $s_\gamma$  and  $|\bar{v}|^2 \cos^2 \theta_\gamma$ .

Note that

$$P_\gamma = \int -s_\gamma \langle |\bar{v}|^2 \cos^2 \theta_\gamma |s_\gamma \rangle P(s_\gamma) ds_\gamma, \quad (4.12)$$

where  $P(s_\gamma)$  is the probability density function (PDF) of  $s_\gamma$ , and  $\langle |\bar{v}|^2 \cos^2 \theta_\gamma |s_\gamma \rangle$  is the conditional average of  $|\bar{v}|^2 \cos^2 \theta_\gamma$  for given  $s_\gamma$ . Therefore, we look into the individual factors on the right-hand side of Eq. (4.12), in particular the conditional average, which provides a measure of the correlation between  $s_\gamma$  and  $|\bar{v}|^2 \cos^2 \theta_\gamma$ .

We show in Fig. 7 the conditional average  $\langle |\bar{v}|^2 \cos^2 \theta_\gamma |s_\gamma \rangle$  for three different  $\eta/\Delta$  (corresponding to  $N_{LES} = 64, 128$  and  $256$ , respectively) and two  $Re_\lambda$  for the case where  $N_{LES} = 256$ . It is clear that the conditional average increases with  $|s_\gamma|$ , which shows that

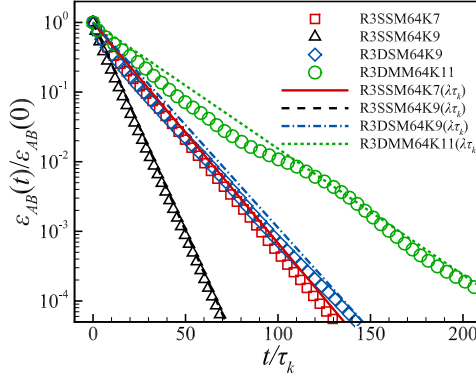


Figure 9: Comparison between the decay rates of the synchronisation error  $\mathcal{E}_{AB}(t)$  and the conditional LLEs of the slave flow.

$|\bar{v}|^2 \cos^2 \theta_\gamma$  is positively correlated with the magnitude of  $s_\gamma$ . More importantly, as  $N_{\text{LES}}$  (hence  $\eta/\Delta$ ) increases, the conditional average increases drastically, especially for larger  $|s_\gamma|$ . Therefore, the correlation between the two enhances quickly with increasing  $\eta/\Delta$ . The weighted conditional average  $-\langle |\bar{v}|^2 \cos^2 \theta_\gamma |s_\gamma \rangle s_\gamma P(s_\gamma)$  is shown in the left panel of Fig. 8. As a consequence of the results in previous figure, the weighted conditional average for higher  $\eta/\Delta$  has a lower but broader peak, which also is located at larger  $|s_\gamma|$ . Because of the broadened peak, the integral of the curve gives a larger value at higher  $\eta/\Delta$ , leading to larger  $P_\gamma$ . The right panel of Fig. 8 plots  $P(s_\gamma)$  for the same cases. The left tails of the PDFs with larger  $N_{\text{LES}}$  (hence larger  $\eta/\Delta$ ) are higher. This also contributes to larger  $P_\gamma$ , but this effect seems to be secondary.

Figs. 5 – 8 show that the changes in  $\lambda\tau_\Delta$  in relation to the Reynolds number come mainly from larger fluctuations in  $s_\gamma$ . This observation is consistent with one of the known effects of small scale intermittency, which is the increased prevalence of large fluctuations in small scale quantities, such as the strain rate tensor, at higher Reynolds numbers (Sreenivasan & Antonia 1997). What these figures show, in addition, is that the alignment between  $\bar{v}$  and the eigenvectors of the strain rate tensor is also positively correlated with the large fluctuations.

#### 4.3. Synchronisation error and its relationship with conditional Lyapunov exponents

We now move onto the discussion of the conditional LLEs and their relationship with the synchronisation between LES. Li *et al.* (2022) shows that, when driven by a DNS (system  $M$ ), two LES (systems  $A$  and  $B$ ) can be synchronised as long as the coupling wavenumber  $k_m$  is sufficiently large. The synchronisation between  $\bar{u}_A$  and  $\bar{u}_B$  can be shown with the synchronisation error

$$\mathcal{E}_{AB}(t) = \|\bar{u}_A - \bar{u}_B\|, \quad (4.13)$$

which decays exponentially when synchronisation happens. However, the relationship between the decay rate and the conditional LLEs was not explored in Li *et al.* (2022). Nikolaidis & Ioannou (2022) and Li *et al.* (2024) showed that the decay rate of the synchronisation error is the same as the conditional LLE, but only for two systems that are directly coupled, not for systems coupled through a third system.

Fig. 9 shows the results for  $\mathcal{E}_{AB}(t)$  with symbols, for selected cases in our numerical experiments that use indirect coupling. The decay of  $\mathcal{E}_{AB}(t)$  on average is exponential for sufficiently large  $k_m$ . The synchronisation can happen with very different rates for different models and different  $k_m$ . These behaviours are the same as those reported in Li *et al.*

(2022).  $\mathcal{E}_{AB}(t)$  is compared with the predictions based on the conditional LLEs, which are shown with the lines without symbols. The lines represent exponential decay, with slopes given by  $\lambda(k_m)\tau_k$ , which is the non-dimensionalized conditional LLE for the slave LES. The agreement shows that on average the error decays exponentially and the non-dimensionalized decay rate can be given by  $\lambda\tau_k$ . Therefore, the synchronisation between two slave LES coupled via a DNS can also be fully characterised by their conditional LLEs, generalising the conclusion drawn in Nikolaidis & Ioannou (2022); Li *et al.* (2024) for direct coupling.

This conclusion already suggests that the synchronisability of two flows is to some extent independent of the coupling method (direct or indirect). Actually, the synchronisability of the slaves is also insensitive to the nature of the master flow. These assertions can be proven by cross-examining the behaviours of  $\mathcal{E}_{AB}$  in carefully designed numerical experiments. However, these assertions show that the synchronisability of a slave flow is fundamentally determined by its intrinsic inter-scale nonlinear interaction, which can be characterised by its conditional LLEs. Therefore, we will now move onto the discussion of the conditional LLEs. The above assertions will be proven later with the data for the conditional LLEs (instead of those for  $\mathcal{E}_{AB}$ ). This approach highlights the central role of the conditional LLEs in understanding various synchronisation phenomena.

#### 4.4. Conditional Lyapunov exponents and the threshold coupling wavenumber

We now present the results for the conditional LLEs  $\lambda(k_m)$ . As is explained previously, two flows can be synchronised only when the conditional LLE is negative. One main question is what is the threshold value  $k_c$ , i.e., the  $k_m$  value for which the conditional LLE is zero. The results for  $k_c$  are one of the main results to be discussed in this subsection.

There are different ways to normalise the results for the conditional LLEs, some providing more insights than others. We will plot  $\lambda(k_m)\tau_\Delta$  ( $\lambda\tau_\Delta$  for short) against  $k_m\Delta_t$ , where  $\Delta_t$  is the effective dissipation length scale defined in Eq. (3.9). The discussion on the threshold wavenumber  $k_c$  to be presented later will demonstrate the benefits of using  $\Delta_t$  to normalise  $k_m$ .

The results for  $\lambda\tau_\Delta$  are plotted in Fig. 10 for cases in subgroups R1, R3, R4, and R5. The results for R2 have been omitted as they only fall somewhere between those of R1 and R3. In all cases  $\lambda\tau_\Delta$  is a decreasing function of  $k_m\Delta_t$ . For the low Reynolds number cases in R1 (top-left) and R3 (top-right), the results for SSM and DSM only change slightly with  $Re_\lambda$  or the filter scale  $\Delta$ . In contrast, those for DMM depend on the two parameters quite significantly. The conditional LLEs for DMM are larger for larger  $\Delta$  (smaller  $N_{LES}$ ), and this effect is the strongest for cases in R3 which have the largest Reynolds numbers.

Data for the high  $Re_\lambda$  cases are shown in the bottom panels of Fig. 10. Different  $Re_\lambda$  and  $\Delta$  lead to different results to some extent, but the difference is not big, and is reduced as  $k_m\Delta_t$  increases. The curves collapse on each other quite well when  $\lambda\tau_\Delta$  approaches zero. This observation implies the threshold wavenumber  $k_c$  for which  $\lambda = 0$  is mostly independent of the Reynolds number, as we will show later.

The threshold wavenumber  $k_c$  can be found from Fig. 10, as it is the value of  $k_m$  for which  $\lambda\tau_\Delta = 0$ . The values are read from the figures directly in the form of  $k_c\Delta_t$ .  $k_c$  can then be recovered and presented in different ways. We start with normalising  $k_c$  with  $\eta$ , and plot  $k_c\eta$  as functions of  $\eta/\Delta$  in Fig. 11. The left panel of the figure can be compared with Fig. 3B in Li *et al.* (2022) where  $k_c\eta$  obtained from the decay rates for the synchronisation error  $\mathcal{E}_{AB}$  is reported. The comparison makes it clear that we obtain essentially the same results, confirming that synchronisation is achievable only when the conditional LLE is negative. To recap briefly the salient features of the curves in the left panel of Fig. 11 (as well as Fig. 3B in Li *et al.* (2022), where the horizontal axis is  $\eta k_\Delta = \pi\eta/\Delta$ ), we note  $k_c\eta$  increases with  $\eta/\Delta$  for SSM and DSM, while it undulates around a value close to 0.2 for DMM. For large

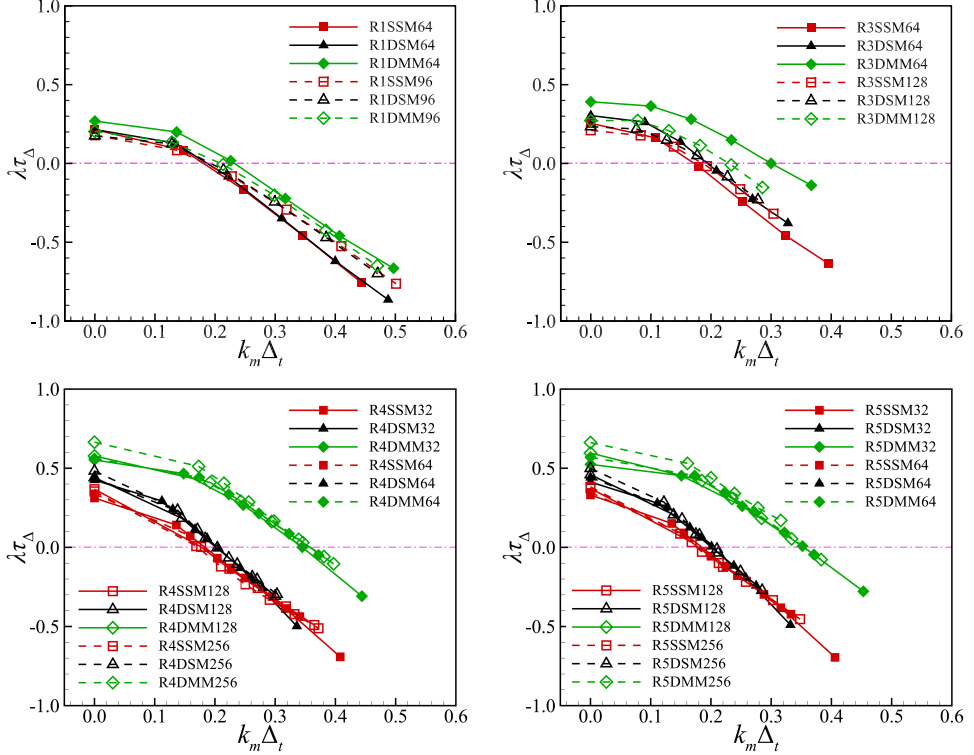


Figure 10: Normalised conditional LLEs  $\lambda\tau_\Delta$  as functions of  $k_m\Delta_t$ . Top-left: R1. Top-right: R3. Bottom-left: R4. Bottom-right: R5.

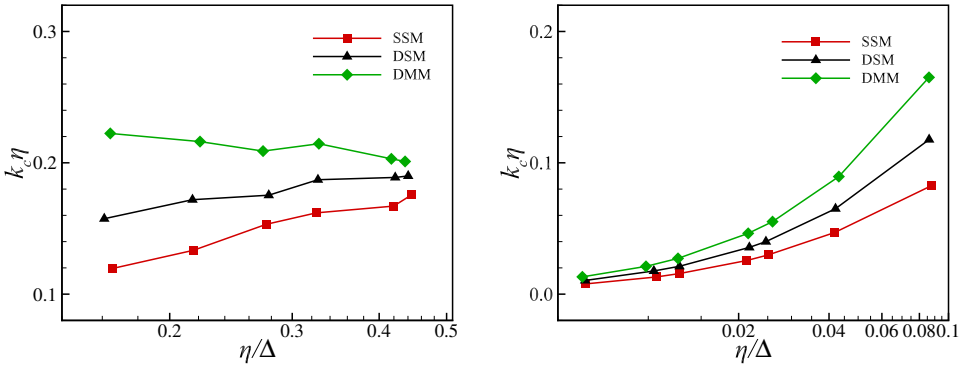


Figure 11: The threshold wavenumber  $k_c\eta$  as a function of  $\eta/\Delta$ . Left: subgroups R1, R2 and R3. Right: subgroups R4 and R5.

$\eta/\Delta$ ,  $k_c\eta$  approaches the DNS value 0.2 (Yoshida *et al.* 2005; Lalescu *et al.* 2013), which is to be expected as  $\Delta \rightarrow \eta$  means the LES approaches the DNS. For a given  $\eta/\Delta$ ,  $k_c\eta$  is the smallest for SSM, somewhat larger for DSM, and the largest for DMM.

The right panel of Fig. 11 complements the results in the left panel with data obtained at higher Reynolds numbers. It shows that, as  $\eta/\Delta$  becomes even smaller,  $k_c\eta$  approaches zero eventually for all models. The behaviour is not surprising, because there is an upper bound for  $k_c$  in LES, but  $\eta$  can approach zero indefinitely as the Reynolds number increases.

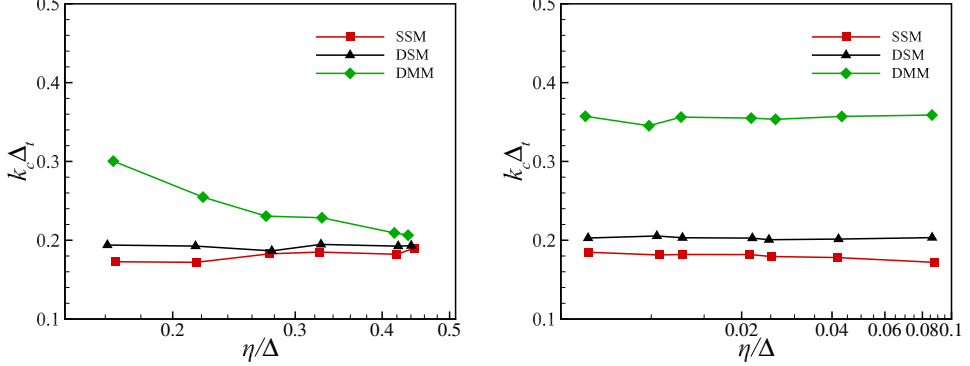


Figure 12: The threshold wavenumber  $k_c \Delta_t$  as a function of  $\eta/\Delta$ . Left: subgroups R1, R2 and R3. Right: subgroups R4 and R5.

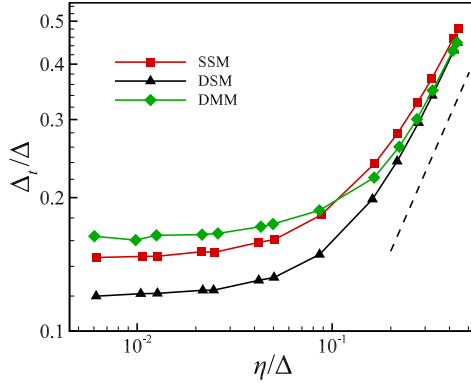


Figure 13:  $\Delta_t/\Delta$  as a function of  $\eta/\Delta$ , with data from all cases in Tables 1 and 2. The dashed line has a slope of 1.

The results in the right panel of Fig. 11 reveal the drawback of the normalisation  $k_c \eta$ , which obscures the difference in  $k_c$  obtained with different models at high Reynolds numbers. This issue is the motivation for the introduction of the length scale  $\Delta_t$ . It turns out that using  $\Delta_t$  to normalise  $k_c$  would lead to more informative results.

We plot  $k_c \Delta_t$  as a function of  $\eta/\Delta$  in Fig. 12, with the left panel showing cases R1 to R3 and the right panel cases R4 and R5. The very interesting observation is that  $k_c \Delta_t$  for both SSM and DSM are almost constant across the whole range of values for  $\eta/\Delta$  covered in both panels. For SSM,  $k_c \Delta_t \approx 0.18$ , and  $k_c \Delta_t \approx 0.20$  for DSM. These values, incidentally, are also close to the DNS value of  $k_c \eta \approx 0.2$ . For DMM,  $k_c \Delta_t$  decreases as  $\eta/\Delta$  increases over the range covered in the left panel, but for smaller  $\eta/\Delta$ , the right panel shows that the value of  $k_c \Delta_t$  levels off and becomes a constant found approximately to be 0.36. Therefore, even though  $k_c \Delta_t$  does not collapse the data for all three models onto one curve, it does have much improved behaviour. For example, based on Fig. 12, we can confidently extrapolate the results to much smaller  $\eta/\Delta$ , whereas it is difficult to do so based on Fig. 11.

To gain more intuition about the above results, it is of interest to understand the behaviour of  $\Delta_t$ . Fig. 13 shows  $\Delta_t/\Delta$  versus  $\eta/\Delta$ . We can see  $\Delta_t/\Delta$  approaches constants as  $\eta/\Delta \rightarrow 0$ . When  $\eta/\Delta \rightarrow 1$ , the curves tend towards  $\Delta_t/\Delta = \eta/\Delta$ , as is shown by the dashed line. Therefore, roughly speaking,  $\Delta_t$  is an interpolation between  $\eta$  and  $\Delta$ , which explains its

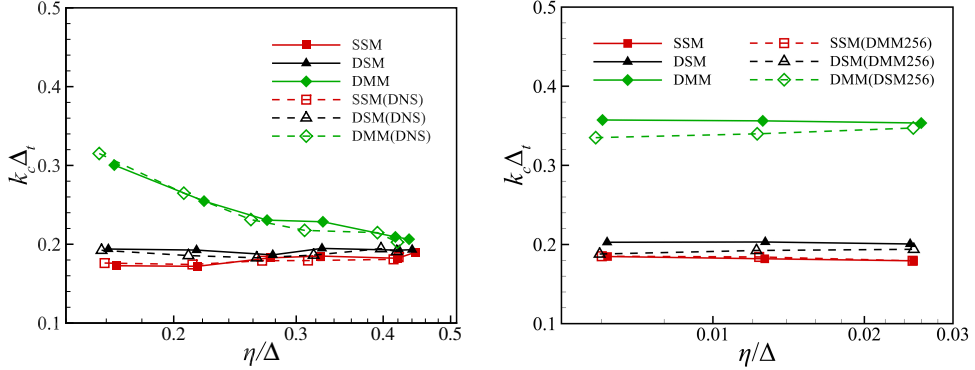


Figure 14: Threshold wavenumber  $k_c \Delta_t$  for synchronisation between two LES driven by indirect coupling via a third system (Dashed lines with empty symbols). Results with direct coupling (i.e. same results in Fig. 12) are shown with solid lines with solid symbols for comparison. Left: indirect coupling via a DNS in subgroups R1, R2 and R3. Right: indirect coupling via a different LES in subgroup R5.

ability to yield a simpler physical picture in  $k_c \Delta_t$  over a wider range of  $\eta/\Delta$ . The asymptotic values for  $\Delta_t/\Delta$  as  $\eta/\Delta \rightarrow 0$  can be read from the figure. Using these values, we can find that, as  $\eta/\Delta \rightarrow 0$ ,  $k_c \Delta$  approaches approximately 0.16, 0.13, and 0.22 for SSM, DSM, and DMM, respectively.

Recall that, in Section 4.3, we assert that different coupling methods and different master systems do not lead to significantly differences in the conditional LLEs. We now present data on  $k_c \Delta_t$  to support this assertion. Fig. 14 compares the threshold wavenumber  $k_c$  obtained with the two coupling methods. The solid lines with solid symbols in this figure are the same as those shown in Fig. 12, which are obtained with direct coupling between two LES, and are included for comparison. The dashed lines with empty symbols are obtained with indirect coupling via a third system (which is the coupling method used in the first set of experiments). For the data shown in the left panel with lower Reynolds numbers, the third system is a DNS. For the high Reynolds number data in the right panel, no DNS at the same Reynolds number is available, therefore an LES with a different SGS stress model is used as the master system. For example, the dashed line with empty squares in the right panel is the results for the synchronisation between two LES with SSM as the SGS stress model, and they are coupled via an  $256^3$  LES with DMM. The main point of Fig. 14 is that the curves for  $k_c \Delta_t$  with indirect coupling follow closely those in Fig. 12, proving our previous assertions. For the sake of brevity, we do not conduct further tests such as LES with DSM as the master system driving LES with SSM, as we expect to observe the same behaviours.

#### 4.5. Threshold wavenumbers and the Lyapunov vectors

In an investigation of the synchronisability of rotating turbulence in a periodic box, Li *et al.* (2024) observed that the threshold wavenumber  $k_c$  is also where the average energy spectrum of the unconditional LLV peaks. The phenomenon is reproduced at different rotation rates and different external forces. In this subsection we investigate whether the phenomenon also exists in non-rotating turbulence simulated with either DNS or LES.

Fig. 15 plots the averaged energy spectra, denoted by  $E_\Delta(k)$ , of the unconditional LLVs in the stationary stage for the DNS velocity in subgroups R1, R2 and R3. As the magnitude of the LLV is irrelevant, the energy spectra have been normalised in such a way that the total energy is unity. For DNS of box turbulence, it is known that the threshold wavenumber  $k_c$  is given by  $k_c \eta \approx 0.2$  (Yoshida *et al.* 2005; Lalescu *et al.* 2013; Inubushi *et al.* 2023). This

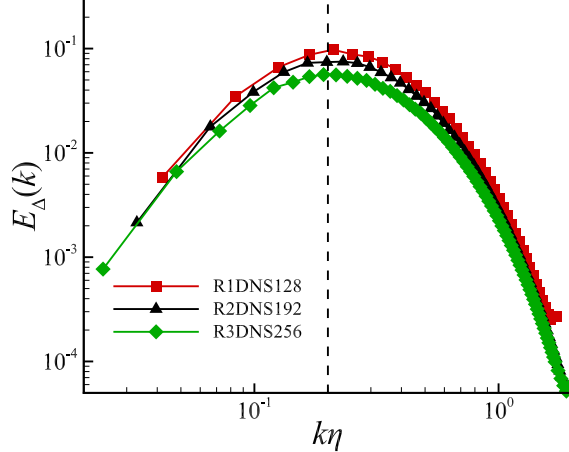


Figure 15: The averaged energy spectra of the unconditional LLV for DNS velocity. The spectra have been normalised such that the total energy is unity.

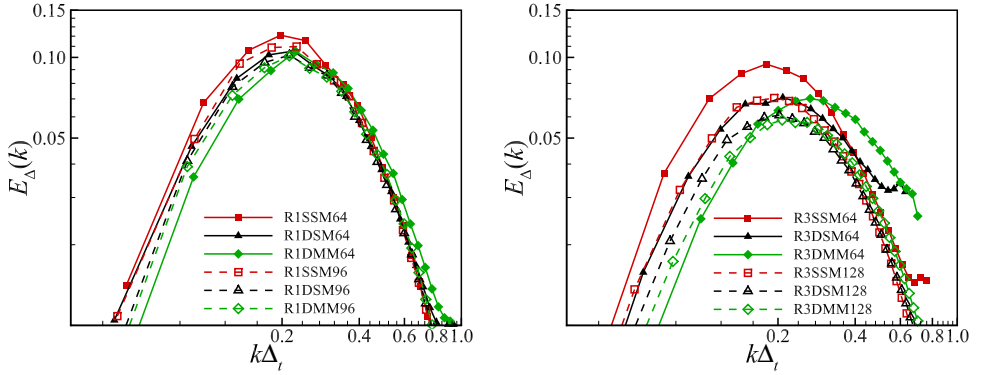


Figure 16: The averaged energy spectra of the unconditional LLV  $\bar{u}^\delta$  for selected LES. Left: subgroups R1. Right: subgroups R3. The spectra have been normalised such that the total energy is unity.

value is marked by the vertical dashed line in Fig. 15. One observe that the spectra do peak approximately at this wavenumber, which verifies the observation in Li *et al.* (2024) in this non-rotating flow.

The results for the LES in Group I are plotted in Fig. 16, including only cases in R1 and R3, two groups of simulations with relatively low Reynolds numbers. Following the normalisation we adopted in previous subsections, the energy spectra are now plotted against  $k\Delta_t$ , where  $\Delta_t$  can be different for different cases. It is clear that the energy spectra also peak at an intermediate wavenumber. That is, the perturbations with energy localised on intermediate wavenumbers are the most unstable. By visual inspection, the peaks of the spectra for both SSM and DSM in different cases are all found around  $k\Delta_t \approx 0.2$ . The same is observed for DMM in most cases, but the most conspicuous exception is case R3DMM64 shown in the right panel, where the peak of the spectra is clearly located at a higher value of  $k\Delta_t$ .

Let the peak wavenumber be  $k_p$ . To compare  $k_p$  with  $k_c$  quantitatively, we need to extract the precise values of  $k_p$  from the spectra. There are challenges for this since the gap between

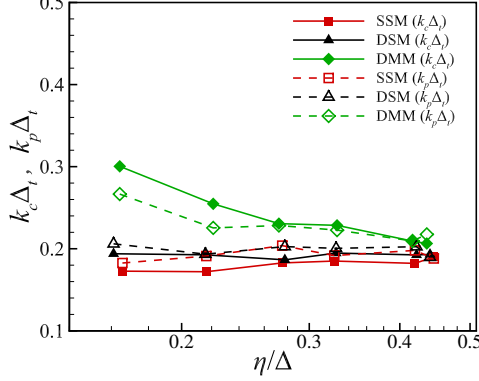


Figure 17: The normalised peak wavenumbers  $k_p \Delta_t$  for cases in subgroups R1, R2 and R3 (dashed lines and empty symbols), compared with  $k_c \Delta_t$  for the same cases (solid lines and solid symbols). The latter is the same as those shown in the left panel of Fig. 12.

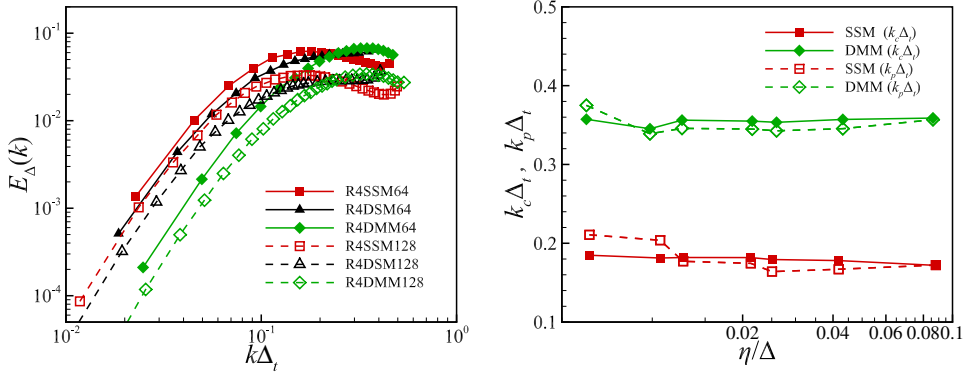


Figure 18: Left: Same as Fig. 16 but for selected cases in subgroup R4. Right: Same as Fig. 17 but for cases in subgroups R4 and R5 and SSM and DMM only.

two data points is fairly large around the peaks. In order to reduce the uncertainty, we use the method in Li *et al.* (2024). Namely, we fit a smooth curve to the spectrum using cubic splines. The peak wavenumber of the fitted curve is taken to be  $k_p$ . More details of the method can be found in Li *et al.* (2024).

The normalised peak wavenumbers  $k_p \Delta_t$  for the LES in R1 - R3 obtained this way are plotted in Fig. 17 together with  $k_c \Delta_t$  from the left panel of Fig. 12 as a comparison. There are some discrepancies between the two quantities, but the overall agreement is good. The discrepancy is somewhat larger for DMM at low  $\eta/\Delta$ , where  $k_p$  is smaller than  $k_c$ . However,  $k_p$ , like  $k_c$ , decreases when  $\eta/\Delta$  increases. Fig. 17 shows that  $k_p$  and  $k_c$ , calculated in entirely different ways, vary with  $\eta/\Delta$  in nearly the same manner. This is strong evidence that the observation made in Li *et al.* (2024) for rotating turbulence is also valid in non-rotating turbulence.

For high Reynolds number cases, we have only LES data. The picture is slightly more complicated, potentially due to the defects in SGS stress models. The left panel of Fig. 18 illustrates the behaviours of the average energy spectra of the unconditional LLVs for selected cases in R4. For SSM and DMM, previous analysis still applies. However, the energy spectra for DSM increase with  $k \Delta_t$  monotonically, therefore have no peak at an

intermediate wavenumber. As a result, the hypothesis fails for high Reynolds number LES with DSM as the SGS stress model.

On the other hand, for SSM and DMM, good quantitative agreement is still observed between  $k_p$  and  $k_c$ . The normalised peak wavenumber  $k_p\Delta_t$  for the two models are shown in the right panel of Fig. 18, which demonstrates the agreement clearly. In particular, the normalised peak wavenumber  $k_p\Delta_t$  for DMM is also approximately 0.36 with only small fluctuations, which appears to be remarkable.

To summarise the findings in this subsection, we argue that there is strong evidence to show that the relationship between the threshold wavenumber and the peak wavenumber is still largely valid in non-rotating box turbulence. For flows with lower Reynolds numbers, we are able to establish this with both DNS and LES supplemented by different SGS stress models. For flows with high Reynolds numbers, we have to use LES due to the limit on computational resources, which leads to uncertain outcomes. We find LES with DSM as the SGS stress model fails to capture this relationship, whereas those with SSM and DMM as the models succeed in doing so.

## 5. Conclusion and discussion

The synchronisation between DNS and LES is investigated via a series of numerical experiments covering different subgrid-scale stress models, Reynolds numbers, coupling methods, and different combinations between the master and the slave flows. By examining the statistics and dynamics of the conditional Lyapunov exponents, the Lyapunov vector, and introducing new parametrisations, we are able to establish the following conclusions.

(i) By calculating the leading Lyapunov exponents for both LES and filtered DNS data, we show both display approximately the same scaling relation with the filter scale  $\Delta$  and qualitatively the same intermittency corrections. This observation provides an interpretation to the Lyapunov exponents for LES as approximations to those of filtered DNS.

(ii) The intermittency corrections to the leading Lyapunov exponents mainly come from the strong correlation between the perturbations and the negative eigenvalue of the strain rate tensor of the underlying turbulent flow.

(iii) The synchronisability of coupled DNS-LES systems or LES-LES systems is mainly determined by the conditional leading Lyapunov exponents of the slave flow itself. To a large extent, it does not depend on the master flow. With the master being either DNS, an LES supplemented with different SGS stress models, or an identical LES, approximately the same conditional leading Lyapunov exponents and threshold coupling wavenumbers  $k_c$  for synchronisation are obtained.

(iv) The peak wavenumber for the averaged energy spectrum of the leading Lyapunov vector is approximately the same as  $k_c$  for both DNS and LES (for certain subgrid-scale stress models), reproducing the observation first reported in rotating turbulence in a periodic box.

(v) The common asymptotic behaviour of  $k_c$  for LES with different models is revealed by introducing an effective dissipation length scale. We show that, as  $\eta/\Delta \rightarrow 0$ , the product  $k_c\Delta$  approaches constant limits for all three different subgrid-scale stress models, with slightly different values for different models.

As some conclusions drawn above are based on LES, which is a model for real flows, additional care is needed when we interpret them. Point (v) above shows that there is fundamental difference between LES and DNS in the context of synchronisation. For DNS of box turbulence, the threshold wavenumber  $k_c$  is expected to be determined by  $k_c\eta = 0.2$ , which means  $k_c \rightarrow \infty$  as  $\eta \rightarrow 0$  at the high Reynolds number limit. This behaviour is different from those observed for all three models. Data for smaller Reynolds numbers

reported previously found that the threshold wavenumber for the dynamic mixed model is approximately the same as that of DNS, but present results unfortunately show that the agreement is not maintained at high Reynolds numbers. Therefore, point (v) serves as a cautionary note for the application of LES in place of DNS in the investigation of synchronisation or in data assimilation experiments. Point (iv) also requires some comments. The relationship is verified in LES with the standard Smagorinsky model and the dynamic mixed model, which we believe provides strong evidence for its general validity. However, to resolve the issue conclusively, DNS with sufficiently large Reynolds numbers is required.

**Funding.** Jian Li acknowledges the support of the National Natural Science Foundation of China (No. 12102391).

**Data availability statement.** The data that support the findings of this study are available from the corresponding author upon reasonable request.

**Declaration of Interests.** The authors report no conflict of interest.

## REFERENCES

BERERA, ARJUN & HO, RICHARD D. J. G. 2018 Chaotic properties of a turbulent isotropic fluid. *Phys. Rev. Lett.* **120**, 024101.

BOCCALETI, S., KURTHS, J., OSIPOV, G., VALLADARES, D. L. & ZHOU, C. S. 2002 The synchronization of chaotic systems. *Phys. Rep.* **366**, 1–101.

BOFFETTA, G., CENCINI, M., FALCIONI, M. & VULPIANI, A. 2002 Predictability: a way to characterize complexity. *Physics Reports* **356**, 367–474.

BOFFETTA, G. & MUSACCHIO, S. 2017 Chaos and predictability of homogeneous-isotropic turbulence. *Phys. Rev. Lett.* **119**, 054102.

BOHR, T., JENSEN, M. H., PALADIN, G. & VULPIANI, A. 1998 *Dynamical Systems Approach to Turbulence*. Cambridge University Press.

BORUE, V. & ORSZAG, S. A. 1996 Numerical study of three-dimensional kolmogorov flow at high reynolds numbers. *J. Fluid Mech.* **306**, 293–323.

BUDANUR, N. B. & KANTZ, H. 2022 Scale-dependent error growth in navier-stokes simulations. *Phys. Rev. E* **106**, 045102.

BUZZICOTTI, M. & LEONI, P. C. De 2020 Synchronizing subgrid scale models of turbulence to data. *Phys. Fluids* **32**, 125116.

DI LEONI, P. C., MAZZINO, A. & BIFERALE, L. 2020 Synchronization to big data: Nudging the navier-stokes equations for data assimilation of turbulent flows. *Phys. Rev. X* **10**, 011023.

FRISCH, U. 1995 *Turbulence: the legacy of A. N. Kolmogorov*. Cambridge universtiy press, Cambridge.

GE, J., ROLLAND, J. & VASSILICOS, J. C. 2023 The production of uncertainty in three-dimensional navier-stokes turbulence. *Journal of Fluid Mechanics* **977**, A17.

GERMANO, M. 1992 Turbulence: the filtering approach. *J. Fluid Mech.* **238**, 325.

HENSHAW, W.D., KREISS, H.-O. & YSTRÓM, J. 2003 Numerical experiments on the interaction between the large- and small-scale motions of the navier–stokes equations. *Multiscale Model. Simul.* **1**, 119–149.

INUBUSHI, M., SAIKI, Y., KOBAYASHI, M. U. & GOTO, S. 2023 Characterizing small-scale dynamics of navier-stokes turbulence with transverse lyapunov exponents: A data assimilation approach. *Physical Review Letters* **131** (25), 254001.

KALNAY, E. 2003 *Atmospheric modelling, data assimilation and predictability*. Cambridge University press, Cambridge.

KANG, H. S., CHESTER, S. & MENEVEAU, C. 2003 Decaying turbulence in an active-grid-generated flow and comparisons with large-eddy simulation. *J. Fluid Mech.* **480**, 129–160.

KUPTSOV, P. V. & PARLITZ, U. 2012 Theory and computation of covariant lyapunov vectors. *J. Nonlinear Sci.* **22**, 727–762.

LALESCU, C. C., MENEVEAU, C. & EYINK, G. L. 2013 Synchronization of chaos in fully developed turbulence. *Phys. Rev. Lett.* **110**, 084102.

LI, J., TIAN, M. & LI, Y. 2022 Synchronizing large eddy simulations with direct numerical simulations via data assimilation. *Phys. Fluids* **34**, 065108.

LI, J., TIAN, M., LI, Y., SI, W. & MOHAMMED, H. K. 2024 The conditional lyapunov exponents and synchronisation of rotating turbulent flows. *J. Fluid Mech.* **983**, A1.

LI, Y., ZHANG, J., DONG, G. & ABDULLAH, N. S. 2020 Small-scale reconstruction in three-dimensional kolmogorov flows using four-dimensional variational data assimilation. *J. Fluid Mech.* **885**, A9.

MENEVEAU, C. & KATZ, J. 2000 Scale-invariance and turbulence models for large-eddy simulation. *Annu. Rev. Fluid Mech.* **32**, 1–32.

NASTAC, G., LABAHN, J. W., MAGRI, L. & IHME, M. 2017 Lyapunov exponent as a metric for assessing the dynamic content and predictability of large-eddy simulations. *Phys. Rev. Fluids* **2**, 094606.

NIKOLAIDIS, M.-A. & IOANNOU, P. J. 2022 Synchronization of low reynolds number plane couette turbulence. *J. Fluid Mech.* **933**.

NIKOLAY, N. 2018 Characteristics of the leading lyapunov vector in a turbulent channel flow. *Journal of Fluid Mechanics* **849**, 942–967.

POPE, S. B. 2000 *Turbulent flows*. Cambridge University Press, Cambridge.

SREENIVASAN, K. R. & ANTONIA, R. A. 1997 The phenomenology of small-scale turbulence. *Annu. Rev. Fluid Mech.* **29**, 435–472.

VELA-MARTIN, A. 2021 The synchronisation of intense vorticity in isotropic turbulence. *J. Fluid Mech.* **913**, R8.

WANG, M. & ZAKI, T. A. 2022 Synchronization of turbulence in channel flow. *J. Fluid Mech.* **943**, A4.

WANG, Y., YUAN, Z. & WANG, J. 2023 A further investigation on the data assimilation-based small-scale reconstruction of turbulence. *Physics of Fluids* **35** (1), 015143.

YOSHIDA, K., YAMAGUCHI, J. & KANEDA, Y. 2005 Regeneration of small eddies by data assimilation in turbulence. *Phys. Rev. Lett.* **94**, 014501.